Monodisperse particle-laden exchange flows in a vertical duct

N. Mirzaeian[1] and K. Alba[1,†]

[1]Department of Engineering Technology, University of Houston, Houston, TX 77204, USA

We study buoyancy-driven exchange flow of two mixtures in a vertical narrow duct (two-dimensional channel as well as pipe) theoretically. While the light mixture is assumed always to be a pure fluid, the heavy mixture can be selected as either a pure or a particle-laden fluid. A small width-to-length ratio considered for the duct ($\delta \ll 1$) has been used as the perturbation parameter in developing a lubrication model (negligible inertia). In particular, we have adopted the methodology of Zhou *et al.* (*Phys. Rev. Lett.*, vol. 94, 2005, 117803) for free-surface particle-laden film flows and extended it to a lock exchange system in confined geometry under the Boussinesq approximation. The resulting model is in the form of the classical Riemann problem and has been solved numerically using a robust total variation diminishing finite difference scheme. Both pure and particle-laden cases are investigated in detail. It is observed that the interface between the two fluids takes a self-similar shape at long times. In the case that both heavy and light fluids are pure, the dynamics of the flow is governed by two dimensionless quantities, namely the Reynolds number, Re, and the viscosity ratio, κ, of the light and heavy fluids. The interpenetration of the heavy and light layers increases with Re but decreases with κ. Also, the heights of the heavy and light fronts change with κ but remain unchanged with Re. In the case of the particle-laden flow, however, four additional dimensionless parameters emerge, namely the initial volume fraction of particles, ϕ_0, the ratio of particle diameter to duct width, r_p, and the density ratios of particles to carrying fluid, ξ, and of light fluid to carrying fluid, η. The effect of these parameters on the dynamics of the flow has been quantified through a systematic approach. In the presence of solid particles, the interface between the heavy and light layers becomes more curved compared to the case of pure fluids. This modification occurs due to the change of heavy mixture viscosity alongside the duct. Novel particle-rich zones are further discovered in the vicinity of the advancing heavy and light fronts. These zones are associated with different transport rates of the fluid and solid particles. The degree of particle enrichment remains the same with Re, is enhanced by κ, r_p and η, and is slightly diminished with ϕ_0 and ξ. On the other hand, the stretched exchange zone between the heavy and light fronts grows with r_p, η and Re, but decays with ϕ_0, κ and ξ.

Key words: multiphase and particle-laden flows, particle/fluid flow

† Email address for correspondence: kalba@uh.edu

1. Introduction

Buoyant interpenetrating flows, due to the release of a heavy mixture into a light one, are amongst the most fundamental fluid mechanics problems widely found in nature within oceanographic, meteorological and geophysical contexts (Benjamin 1968; Shin, Dalziel & Linden 2004; Birman *et al.* 2007). They also have numerous applications in industry, such as in continuous reactors and countercurrent extraction columns (Pratt & Baird 1983; Baird *et al.* 1992). These multiphase flows have been widely studied in the literature, experimentally by Debacq *et al.* (2001), Seon *et al.* (2005, 2007*a*), Znaien, Moisy & Hulin (2011) and Alba, Taghavi & Frigaard (2012, 2013*a*), computationally by Sahu & Vanka (2011), Taghavi, Alba & Frigaard (2012*a*), Alba, Taghavi & Frigaard (2014), Hallez & Magnaudet (2015) and Sebilleau, Issa & Walker (2016) and analytically by Seon *et al.* (2007*b*), Taghavi *et al.* (2009, 2012*b*), Kerswell (2011), Borden & Meiburg (2013) and Alba, Taghavi & Frigaard (2013*b*), considering a pair of pure fluids. Depending on the flow configuration and parameters, various viscous, transitory and diffusive regimes, governed by the balance of viscous, buoyant and inertial forces, may emerge, as laid out by Seon *et al.* (2006), Sahu & Vanka (2011) and Alba *et al.* (2013*a*). In many practical situations, however, the involved fluids are particle-laden (suspension) and therefore not pure. Particle-laden flows have been studied in the literature only in the context of Boycott flow (settlement-induced convection within a single suspension mixture) by Boycott (1920) and Davis, Herbolzheimer & Acrivos (1983), turbidity currents (intrusion of a suspension into a liquid ambient over a nearly horizontal free-surface geometry) by Bonnecaze, Huppert & Lister (1993) and Meiburg & Kneller (2010), and debris flows (intrusion of a suspension into a gas ambient over an incline) by Cook (2008), Cook, Bertozzi & Hosoi (2008) and Wang *et al.* (2015). The interpenetrating exchange flow of a suspension into another fluid in a practical duct geometry has received very little attention in the literature due to the increased complexity arising from the interaction of the solid–fluid as well as fluid–fluid phases within enclosed walls. One of the few studies available in the literature on this topic is the recent work of Saha, Salin & Talon (2013) carried out experimentally for a horizontal configuration. Numerous applications of particle-laden interpenetrating flows are found in a variety of industrial operations, such as discharge, transport and dispersion of slurries, mine tailings, pastes, pharmaceuticals, paper pulp, drill cuttings, sludge, effluents and sewage, also the manufacture of cement clinker in inclined kilns, mineral processing in hydrocyclones, and fluidized beds, as discussed by Segre & Silberberg (1961), Asomah & Napier-Munn (1997), Hamed (2005), Nelson & Guillot (2006), Wiklund *et al.* (2006) and Boateng (2015).

The lubrication approximation can be applied to model flows in the buoyant viscous domain with negligible inertia. A continuum one-dimensional lubrication model of a particle-laden film flowing down a slope was first developed by Zhou *et al.* (2005), predicting the evolution of the interface height, h, and particle volume fraction, ϕ, with time, t, and streamwise distance, x. Zhou *et al.* (2005), Cook (2008) and Cook *et al.* (2008) reported the formation of a particle-rich ridge in the vicinity of the advancing suspension front (contact line) due to the different rates of solid and fluid transport. Two-dimensional (2D) effects were later studied by Cook, Alexandrov & Bertozzi (2009), revealing that the addition of solid particles can diminish the well-known fingering instabilities of an advancing contact line. While there is a large body of studies on modelling single-layer suspension film flows, the literature on two-layer exchange systems of suspension and pure fluid is severely lacking. As a novel approach, we extend the methodology of Zhou *et al.* (2005) for free-surface
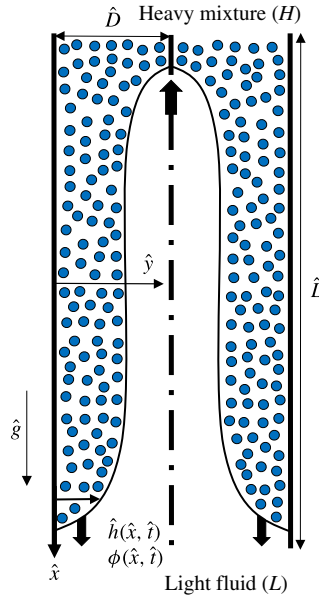
FIGURE 1. (Colour online) Schematic of the symmetric particle-laden exchange flow in a vertical 2D duct used in the lubrication model analysis. Note that dimensional notations are used in the figure. The interface shape is illustrative only.

film flows to a practical exchange system within a confined (duct) geometry. As discussed by Kerswell (2011), the exchange flow of two fluids in a vertical duct may reveal slumping side-by-side or symmetric patterns with either heavy or light fluids moving in the core region of the duct. In particular, we are interested in the symmetric mode where the heavy particle-laden film falls along the side walls and the light fluid moves upwards in the centre of the duct; see figure 1. From a different perspective, the examined exchange flow can be considered as an extension to the fundamental Taylor bubble problem of Davies & Taylor (1950), now studied for particle-laden fluids.

The important dimensional and dimensionless parameters of the problem are first laid out in § 2. The lubrication model is then derived in § 3. A total variation diminishing (TVD) finite difference scheme, used to numerically solve the derived model, is explained in § 4. In the presentation of our results in § 5, we first discuss the case of pure fluids and then examine the effect of particle addition to the flow. The effects of a wide range of controlling parameters, such as the density, size and volume fraction of particles, as well as the viscosity and density of the light and carrying fluids, and the Reynolds number, are investigated in detail. The paper closes with a brief summary in § 6. A last note here is that the model developed in this paper is unable to capture interfacial instabilities due to the inherent lubrication model assumption used (negligible inertia). This model is only applicable to highly viscous regimes with negligible inertia (Taghavi *et al.* 2009). The authors have extensively studied the stability of thin pure fluid films in their previous works, such as in Alba, Laure & Khayat (2011), Taghavi *et al.* (2012b) and Alba *et al.* (2013b), via a weighted residual (WR) model. Extending the current particle-laden formulation to a similar WR model, capable of capturing instabilities, is extremely challenging due to the addition of weakly inertial terms in the Navier–Stokes equations.

2. Dimensional and dimensionless governing parameters

The problem shown schematically in figure 1 involves 11 dimensional parameters, which we denote with the ˆ symbol. The gravitational acceleration is denoted by $\hat{g}$. The vertical duct has width, $2\hat{D}$, and length, $\hat{L}$. The duct geometry considered may simulate particle-laden groundwater flows through aquifers, conduits, caves, cracks, joints and faults. To capture the fully developed flow effects as discussed by Alba *et al.* (2013*a*), we assume $\hat{L} \gg \hat{D}$. The solid particles, which are considered to be heavier than the carrying fluid (negatively buoyant), have radius $\hat{a}$ and density $\hat{\rho}_p$. In particular, we are interested in non-Brownian suspensions, i.e. $\hat{a} > 1$ μm (Espín & Kumar 2014). The Newtonian carrying fluid in the heavy solution has density $\hat{\rho}_{f,H}$ and viscosity $\hat{\mu}_{f,H}$. Similarly, the Newtonian light fluid density and viscosity are denoted by $\hat{\rho}_L$ and $\hat{\mu}_L$, respectively. Both the fluids and solid phases are assumed to be incompressible. The initial total volume of particles is $\hat{V}_p$. At time $\hat{t} = 0$ s, the heavy particle-laden mixture occupies the top half of the duct ($\hat{x} < 0$) whereas the light pure fluid takes up the bottom half ($\hat{x} \geqslant 0$). The jamming volume, which depends on the shape and packing arrangement of the particles, is further designated by $\hat{V}_j$ (Saha *et al.* 2013). Through a dimensional analysis based on Buckingham's π theorem, it is not difficult to show that eight dimensionless parameters control the flow in question, namely the duct aspect ratio, $\delta = \hat{D}/\hat{L} \ll 1$, particle-radius-to-half-duct-width ratio, $r_p = \hat{a}/\hat{D}$, particle-to-carrying-fluid density ratio, $\xi = \hat{\rho}_p/\hat{\rho}_{f,H}$, light-to-carrying-fluid density ratio, $\eta = \hat{\rho}_L/\hat{\rho}_{f,H}$, light-to-carrying-fluid viscosity ratio, $\kappa = \hat{\mu}_L/\hat{\mu}_{f,H}$, initial volume fraction of particles, $\phi_0 = \hat{V}_p/\hat{V}_H$, jamming volume fraction, $\phi_j = \hat{V}_j/\hat{V}_H$, and the Reynolds number, $Re = \hat{\rho}_H(\phi_0)\hat{V}_t(2\hat{D})/\hat{\mu}_H(\phi_0)$. Similar to the approach of Cook *et al.* (2008), we assume that the volume fraction of particles across the depth of the suspension layer, y, is uniform, i.e. $\phi = \phi(x, t)$ only. See Metzger, Guazzelli & Butler (2005) for particle heterogeneity effects in sedimentary flows and appendix A for negligibility of shear-induced migration effects. Assuming that the duct has unit depth, the total volume of the heavy solution is found as $\hat{V}_H = \hat{D}\hat{L}$. Further assuming monodisperse spherical particles, the jamming volume fraction is obtained as $\phi_j \approx 0.67$ (Cook *et al.* 2008). The expressions $\hat{\rho}_H(\phi_0) = \hat{\rho}_p\phi_0 + \hat{\rho}_{f,H}(1 - \phi_0)$ and $\hat{\mu}_H(\phi_0) = \hat{\mu}_{f,H}(1 - \phi_0/\phi_j)^{-2}$ determine the density and viscosity of the heavy fluid, respectively (Saha *et al.* 2013). The characteristic velocity in the Reynolds-number expression is defined as $\hat{V}_t = \sqrt{(1 - \psi)\hat{g}\hat{D}/(1 + \psi)}$, where $\psi = \hat{\rho}_L/\hat{\rho}_H(\phi_0) = \eta/(1 + (\xi - 1)\phi_0)$ is the density ratio of the light fluid to the heavy suspension. In our simulations, η can be larger than 1, i.e. the light fluid heavier than the carrying fluid. However, ψ is always less than 1, meaning that the overall suspension mixture is heavier than the light fluid. The dimensional parameters governing the flow along with the dimensionless numbers and their ranges are listed in tables 1 and 2.

3. Lubrication model derivation

We aim to construct a lubrication model in simplified vertical 2D channel geometry, shown schematically in figure 1. Owing to symmetry, only half of the duct domain between the left wall ($y = 0$) and centre ($y = 1$) is considered in the model. Extending the model to a pipe geometry, potentially more convenient for experimentation, is performed in appendix B. As discussed in depth in appendix A, for the Boussinesq limit considered ($At \ll 1$ where $At = (\hat{\rho}_H(\phi_0) - \hat{\rho}_L)/(\hat{\rho}_H(\phi_0) + \hat{\rho}_L) = (1 - \psi)/(1 + \psi)$

Definition	Parameter
Gravitational acceleration	$\hat{g}$
Half duct width	$\hat{D}$
Duct length	$\hat{L}$
Particle radius	$\hat{a}$
Particle density	$\hat{\rho}_p$
Carrying fluid density	$\hat{\rho}_{f,H}$
Carrying fluid viscosity	$\hat{\mu}_{f,H}$
Light fluid density	$\hat{\rho}_L$
Light fluid viscosity	$\hat{\mu}_L$
Initial total volume of particles	$\hat{V}_p$
Jamming volume of particles	$\hat{V}_j$

TABLE 1. List of dimensional independent input parameters of the problem.

Definition	Parameter
Aspect ratio	$\delta = \hat{D}/\hat{L} \ll 1$
Particle-radius-to-half-duct-width ratio	$r_p = \hat{a}/\hat{D} \ll 1$
Particle-to-carrying-fluid density ratio	$\xi = \hat{\rho}_p/\hat{\rho}_{f,H} > 1$
Light-to-carrying-fluid density ratio	$\eta = \hat{\rho}_L/\hat{\rho}_{f,H} > 1$
Light-to-carrying-fluid viscosity ratio	$\kappa = \hat{\mu}_L/\hat{\mu}_{f,H} \in [0.1, 10]$
Initial volume fraction of particles	$\phi_0 = \hat{V}_p/\hat{V}_H < \phi_j$
Jamming volume fraction of particles	$\phi_j = \hat{V}_j/\hat{V}_H \approx 0.67$
Reynolds number	$Re = \hat{\rho}_H(\phi_0)\hat{V}_t(2\hat{D})/\hat{\mu}_H(\phi_0) \sim O(1)$

TABLE 2. List of dimensionless independent input parameters of the problem.

is the Atwood number), we may neglect the diffusive effects associated with shear-induced migration of particles (Cook *et al.* 2008; Mavromoustaki & Bertozzi 2014; Wang & Bertozzi 2014). A lubrication model describing viscous exchange flow of pure fluids has been developed in our recent work (Hasnain & Alba 2017) for which the configuration was considered to be slumping, i.e. no-slip condition at both $y = 0$ and 1. Here, we adopt a *symmetric* configuration, i.e. no-slip condition at $y = 0$ and stress-free condition at $y = 1$. Following the approach of Hasnain & Alba (2017), the governing streamwise and depthwise momentum equations in the heavy particle-laden layer reduce to

$$0 = -p_x + \frac{\rho_H(\phi)Re}{1 - \psi} + \mu_H(\phi)u_{yy}, \tag{3.1}$$

$$0 = -p_y, \tag{3.2}$$

where we have scaled the streamwise and depthwise distances by $\hat{D}/\delta$ and $\hat{D}$, respectively. Moreover, the pressure has been scaled by $\hat{\mu}_H(\phi_0)\hat{V}_t/\delta\hat{D}$. The dimensionless density and viscosity of the heavy layer in the continuum form and as a function of the particle volume fraction, ϕ, are expressed as (Cook *et al.* 2008)

$$\rho_H(\phi) = \frac{1 + (\xi - 1)\phi}{1 + (\xi - 1)\phi_0}, \tag{3.3}$$

$$\mu_H(\phi) = \frac{(1 - \phi/\phi_j)^{-2}}{(1 - \phi_0/\phi_j)^{-2}}. \tag{3.4}$$

Similarly, for the light fluid layer we obtain

$$0 = -p_x + \frac{\psi Re}{1-\psi} + m u_{yy}, \tag{3.5}$$

$$0 = -p_y, \tag{3.6}$$

where $m = \hat{\mu}_L/\hat{\mu}_H(\phi_0) = \kappa(1 - \phi_0/\phi_j)^2$ is the viscosity ratio of the light fluid to that of the heavy suspension layer. Integrating (3.2) and (3.6) across the width gives

$$p = p_0(x, t) + \frac{\rho_H(\phi)xRe}{1-\psi}, \quad 0 \leqslant y \leqslant 1, \tag{3.7}$$

where we define $p_0(x, t)$ as

$$p_0(x, t) = p(x, 0, t) - \frac{\rho_H(\phi)xRe}{1-\psi}. \tag{3.8}$$

In obtaining (3.7), we neglected the effects of interfacial tension between the two mixtures for simplicity. In other words, we consider an immiscible interface but with zero interfacial tension. Such a limit is indeed equivalent to a miscible interface with zero molecular diffusion; see Petitjeans & Maxworthy (1996), Taghavi *et al.* (2012*b*) and Alba *et al.* (2013*b*) for studies taking a similar approach for pure fluids.

The pressure expression (3.7) is now used in the streamwise momentum equations (3.1) and (3.5) to give

$$0 = -P_{0,x} + \mu_H(\phi)u_{yy}, \quad 0 \leqslant y \leqslant h, \tag{3.9}$$

$$0 = -P_{0,x} - \frac{\rho_H(\phi) - \psi}{1-\psi}Re + m u_{yy}, \quad h \leqslant y \leqslant 1. \tag{3.10}$$

Note that, for simplification, we have defined $P_{0,x} = p_{0,x} + (x\rho_{H,\phi}\phi_x Re)/(1 - \psi)$. Applying appropriate boundary and interfacial conditions in (3.11)–(3.13), the equations (3.9) and (3.10) can be integrated with respect to y in order to determine the streamwise velocity closures in each layer. In the case of miscible fluids, a standard no-slip condition at the lower wall ($y = 0$) may be used. However, in the case of immiscible fluids, we face the well-known contact-line problem due to the singularity of the stress at the walls. Many authors have worked intensely for decades to address this issue, suggesting a wide range of remedies, e.g. replacing no-slip conditions at the wall by Navier slip ones (Greenspan 1978), assuming a narrow precursor film of thickness b in the vicinity of the wall as laid out by Spaid & Homsy (1996), etc. As mentioned in § 1, similar to Cook *et al.* (2008) we are interested in a scenario where the suspension mixture flows close to the surface of the duct wall. The precursor film approach then suits our application best. In fact, the validity of such an assumption for particle-laden flows has been confirmed in the experiments of Zhou *et al.* (2005). Owing to the symmetry, we can further apply the stress-free condition in the duct centre ($y = 1$). In summary, we have

$$u = 0, \quad \text{at } y = 0, \tag{3.11}$$

$$u_y = 0, \quad \text{at } y = 1. \tag{3.12}$$

The homogeneity of the velocity and stress at the interface, h, requires

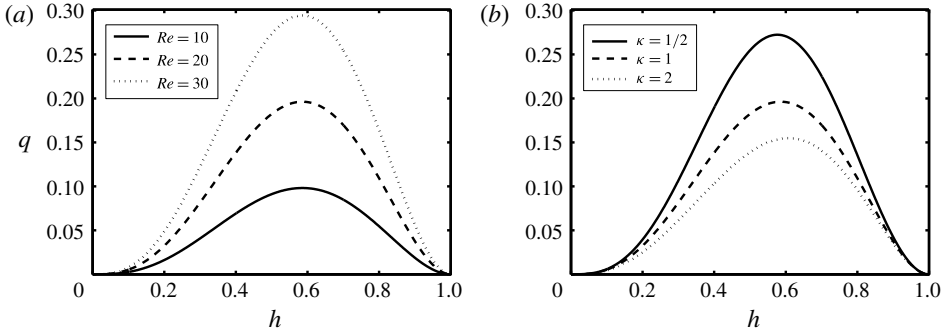$$[u] = 0, \quad [\tau_{xy}] = 0, \quad \text{at } y = h, \tag{3.13a,b}$$

FIGURE 2. Variation of the flux function, q, in (3.17) with interface height, h, for pure fluids ($\phi_0 = r_p = \xi = 0$) and (a) $\kappa = 1$ at various values of Re, and (b) $Re = 20$ at various values of κ. Owing to the choice of scaling used, the results in the pure fluids limit do not depend on η.

where [ ] denotes the jump of the given quantity. Note that in (3.13), $\tau_{xy} = u_y$ for the heavy and $\tau_{xy} = mu_y$ for the light fluids, respectively. The last condition needed to solve the system of equations (3.9) and (3.10) for the velocity closures is the total flow constraint,

$$\int_0^1 u \, dy = 0. \tag{3.14}$$

The streamwise velocity, u, in the heavy and light layers can then be obtained by integrating (3.9) and (3.10) twice as

$$u = \frac{P_{0,x} y^2}{2\mu_H} + c_1 y + c_2, \quad 0 \leqslant y \leqslant h, \tag{3.15}$$

$$u = \left(P_{0,x} + \frac{\rho_H - \psi}{1 - \psi} Re \right) \frac{y^2}{2m} + d_1 y + d_2, \quad h \leqslant y \leqslant 1, \tag{3.16}$$

where $P_{0,x}$, c_1, c_2, d_1 and d_2 are coefficients given in appendix C. The flux function, $q = \hat{q}/\hat{D}$, as the flow rate within the heavy layer can eventually be calculated as

$$q = \int_0^h u \, dy, \tag{3.17}$$

which is given in appendix D as a function of h, Re, m, μ_H and ρ_H. In the case of pure fluids ($\phi_0 = 0$), we obtain $\rho_H = \mu_H = 1$ from (3.3) and (3.4). The relevant dimensionless numbers governing the flow would then be reduced to Re and κ. Note that, since $\rho_H = 1$ in (3.16), the model becomes independent of ψ (thus η). Figures 2(a) and 2(b) show the variation of q versus h for different values of Re and κ, respectively. As $h \to 0$ and 1, $q \to 0$. The flux function q exhibits a maximum in the interval $h \in [0, 1]$. The location of this maximum remains unchanged in the iso-viscous case, $h \approx 0.586$; see figure 2(a). However, the maximal q location shifts slightly to the left (smaller h) with decreasing viscosity ratio, κ, i.e. less viscous light fluid, as shown in figure 2(b).

The evolution equations for the interface height and particle volume fraction, respectively, read (see also Cook *et al.* (2008) for a similar formulation derived for particle-laden film flow over an inclined surface)

$$h_t + q_x = 0, \tag{3.18}$$

$$(\phi h)_t + (u_p \phi h)_x = 0, \tag{3.19}$$

where u_p is the particle velocity expressed as $u_p = q/h + u_s(1 - \phi)$. Here, $u_s = f(\phi)w(h)u_0$ is the dimensionless hindered Stokes velocity, with $u_0 = 2\hat{a}^2(\hat{\rho}_p - \hat{\rho}_{f,H})\hat{g}/ (9\hat{V}_t\hat{\mu}_{f,H})$ or $u_0 = (\xi - 1)\psi\kappa Re(1 + \psi)r_p^2/(9m\eta(1 - \psi))$ being the dimensionless Stokes velocity of a single particle (Saha *et al.* 2013). Moreover, $f(\phi) = (1 - \phi)^5$ is the Richardson–Zaki settling function (Richardson & Zaki 1954) and $w(h)$ is the wall function chosen as $w(h) = h^2$ to give 0 and 1 at the wall ($y = 0$) and centre ($y = 1$), respectively; see also Cook *et al.* (2008) for other forms of the wall function. In (3.18) and (3.19), time is naturally scaled by $\hat{D}/\delta\hat{V}_t$. In order to advantageously solve the system of equations (3.18) and (3.19) in a conservative framework, we define an additional parameter θ as

$$\theta = \phi h. \tag{3.20}$$

Using (3.20), (3.18) and (3.19) will result in the following set of equations, simply in the form of a classical Riemann problem,

$$h_t + F_x(h, \theta) = 0, \tag{3.21}$$

$$\theta_t + G_x(h, \theta) = 0, \tag{3.22}$$

where

$$F(h, \theta) = q(h, \theta), \tag{3.23}$$

$$G(h, \theta) = \frac{\theta F(h, \theta)}{h} + u_0\theta \left(1 - \frac{\theta}{h}\right) f\left(\frac{\theta}{h}\right) w(h). \tag{3.24}$$

The kinematic conditions (3.21) and (3.22) along with flux condition (3.14) ensure conservation of pure fluids as well as total mass of particles (and thus volume and area due to the presumed incompressibility) at all times.

4. Numerical scheme

4.1. *Procedure*

Our methodology to numerically solve the system of partial differential equations (PDEs) of (3.21) and (3.22) in space x and time t is based on the robust explicit high-resolution TVD finite difference scheme of Kurganov & Tadmor (2000). We first define

$$\boldsymbol{u} = \begin{bmatrix} h \\ \theta \end{bmatrix}, \quad \boldsymbol{f} = \begin{bmatrix} F \\ G \end{bmatrix}. \tag{4.1a,b}$$

Discretizing (3.21) and (3.22) using the finite difference method gives

$$\frac{\boldsymbol{u}_j^{n+1} - \boldsymbol{u}_j^n}{\Delta t} + \frac{1}{\Delta x} \left[\boldsymbol{f}_{j+1/2}^n - \boldsymbol{f}_{j-1/2}^n\right] = 0. \tag{4.2}$$

The flux vector, $\boldsymbol{f}$, in (4.2) is expressed as

$$\boldsymbol{f}_{j\pm1/2}^{n} = \tfrac{1}{2}\left\{\left[\boldsymbol{f}\left(\boldsymbol{u}_{j\pm1/2}^{R,n}\right) + \boldsymbol{f}\left(\boldsymbol{u}_{j\pm1/2}^{L,n}\right)\right] - a_{j\pm1/2}^{n}\left[\boldsymbol{u}_{j\pm1/2}^{R,n} - \boldsymbol{u}_{j\pm1/2}^{L,n}\right]\right\}. \tag{4.3}$$

Here,

$$\left.\begin{aligned}
\boldsymbol{u}_{j+1/2}^{R,n} &= \boldsymbol{u}_{j+1}^{n} - \frac{\Delta x}{2}(\boldsymbol{u}_{x}^{n})_{j+1}, \quad \boldsymbol{u}_{j+1/2}^{L,n} = \boldsymbol{u}_{j}^{n} + \frac{\Delta x}{2}(\boldsymbol{u}_{x}^{n})_{j}, \\
\boldsymbol{u}_{j-1/2}^{R,n} &= \boldsymbol{u}_{j}^{n} - \frac{\Delta x}{2}(\boldsymbol{u}_{x}^{n})_{j}, \quad \boldsymbol{u}_{j-1/2}^{L,n} = \boldsymbol{u}_{j-1}^{n} + \frac{\Delta x}{2}(\boldsymbol{u}_{x}^{n})_{j-1},
\end{aligned}\right\} \tag{4.4}$$

with $(\boldsymbol{u}_{x}^{n})_{k}$ being a flux limiter chosen to be in the minmod class of the following form:

$$(\boldsymbol{u}_{x}^{n})_{k} = \text{minmod}\left(\frac{\boldsymbol{u}_{k}^{n} - \boldsymbol{u}_{k-1}^{n}}{\Delta x}, \frac{\boldsymbol{u}_{k+1}^{n} - \boldsymbol{u}_{k}^{n}}{\Delta x}\right). \tag{4.5}$$

The minmod function is defined as

$$\text{minmod}(a, b) = \tfrac{1}{2}[\text{sgn}(a) + \text{sgn}(b)]\min(|a|, |b|). \tag{4.6}$$

Also note that

$$a_{j\pm1/2}^{n} = \max\left[\rho\left(\frac{\partial \boldsymbol{f}}{\partial \boldsymbol{u}}\right)_{\boldsymbol{u}_{j\pm1/2}^{R,n}}, \rho\left(\frac{\partial \boldsymbol{f}}{\partial \boldsymbol{u}}\right)_{\boldsymbol{u}_{j\pm1/2}^{L,n}}\right] \tag{4.7}$$

gives the local propagation speed of the interfacial wave. Here,

$$\rho(\boldsymbol{A}) = \max(|\lambda_{1}|, |\lambda_{2}|) \tag{4.8}$$

is the spectral radius of matrix $\boldsymbol{A}$, with λ_{1} and λ_{2} being its eigenvalues. The stable time step, $\text{d}t$, is calculated using a Courant–Friedrichs–Lewy (CFL) condition as

$$\text{d}t = \frac{CFL\,\text{d}x}{\max(|a(t)|)}. \tag{4.9}$$

For our simulations, we have found that $CFL \approx 0.1$ leads to stable results. Once h and θ are computed, the particle volume fraction can be simply obtained from $\phi = \theta/h$. The numerical examples shown in this paper are attained using the computational resources in the Center for Advanced Computing & Data Systems of the University of Houston (Maxwell cluster). While the run-time on a parallelized code on such a cluster (four nodes) for pure fluids can be very quick (order of minutes), due to the extremely small mesh size required in the particle-laden case, it can take up to four days for the simulations to complete. We will discuss this in more detail in §5.2.

4.2. *Benchmarking notes*

In order to ensure the validity of our model and numerical scheme, the following steps were taken (results are not presented here for brevity). (1) Figures 6.23–6.27 and 6.32 in Kurganov & Tadmor (2000), obtained from solving similar nonlinear conservation equations to (3.21) and (3.22), were successfully recovered using our code. (2) Adopting the flux function expression given in appendix B of

Hasnain & Alba (2017), we benchmarked their results of exchange flow of pure immiscible fluids in a duct. (3) In the case of particle-laden film flow over a flat free surface studied by Cook *et al.* (2008), the flux function, q, is shown to simply reduce to $q = \rho_H h^3 / \mu_H$; compare with the expression for q given in our appendix D. Using this flux function and our numerical scheme, we fully recovered figures 4.3 and 4.4 in Cook *et al.* (2008), where they depict particle enrichment and depletion effects in the vicinity of the advancing suspension front. We will discuss this issue in detail in § 5.2.

5. Results

5.1. *Pure fluids* ($\phi_0 = 0$)

While the slumping exchange flow of two fluids in a duct has been investigated extensively in the literature (Taghavi *et al.* 2009; Martin *et al.* 2011; Matson & Hogg 2012; Hasnain & Alba 2017), the symmetric configuration, to the best of our knowledge, has not been studied even for pure fluids. Therefore, we find it important to address such a limit first before moving on to a more complicated particle-laden flow. In the absence of an interfacial tension between the two fluids, the thickness of the precursor film can be chosen as zero ($b = 0$) without any contact-line singularity issue (Taghavi *et al.* 2009; Hasnain & Alba 2017). Figure 3(*a*) shows the evolution of the interface height with time assuming two iso-viscous fluids ($\kappa = 1$) at $Re = 20$. The initial condition is such that the interface height is $h = 1$ and 0 over $x < 0$ and $x \geqslant dx$, respectively, i.e. the heavy (light) mixture occupying the left (right) side of the duct. It has been confirmed that the computed solution is not sensitive to the choice of initial conditions (results not presented here for brevity). The mesh size chosen to produce figure 3(*a*) and all other pure fluid examples is $dx = 0.02$. The results for $dx = 0.002$ are almost indistinguishable from those of $dx = 0.02$, as illustrated in figure 3(*a*). Owing to the symmetric duct flow configuration, the light layer in the centre of the duct has to advance faster than the heavy one to conserve mass.

The interface profiles shown in figure 3(*a*) suggest a rather self-similar pattern in the form of steady travelling waves. Using a similarity parameter, $\lambda = x/t$, equation (3.18) can be rewritten as

$$-\frac{\lambda h_\lambda}{t} + \frac{q_\lambda}{t} = 0. \tag{5.1}$$

Alternatively, the following condition can be derived:

$$\lambda = q_h, \tag{5.2}$$

which, via the expression for q given in appendix D, relates λ to h, Re and κ. For the example shown in figure 3(*a*) ($\phi_0 = 0$, $Re = 20$, $\kappa = 1$), we may obtain the following:

$$\lambda = -10(h^3 - 5h^2 + 6h - 2)h^2. \tag{5.3}$$

Equation (5.3) clearly has an analytical expression for h as a function of λ. However, it can be checked that this solution does not satisfy the total flow rate constraint (3.14) over the whole range of λ (Hasnain & Alba 2017). Zheng, Rongy & Stone (2015) showed that a compound wave solution may instead be put forth comprising heavy and light layer front heights, h_{Hf} and h_{Lf}, located at λ_{Hf} and λ_{Lf}, respectively; and a stretching region in between ($\lambda_{Lf} < \lambda < \lambda_{Hf}$). Following the approach of
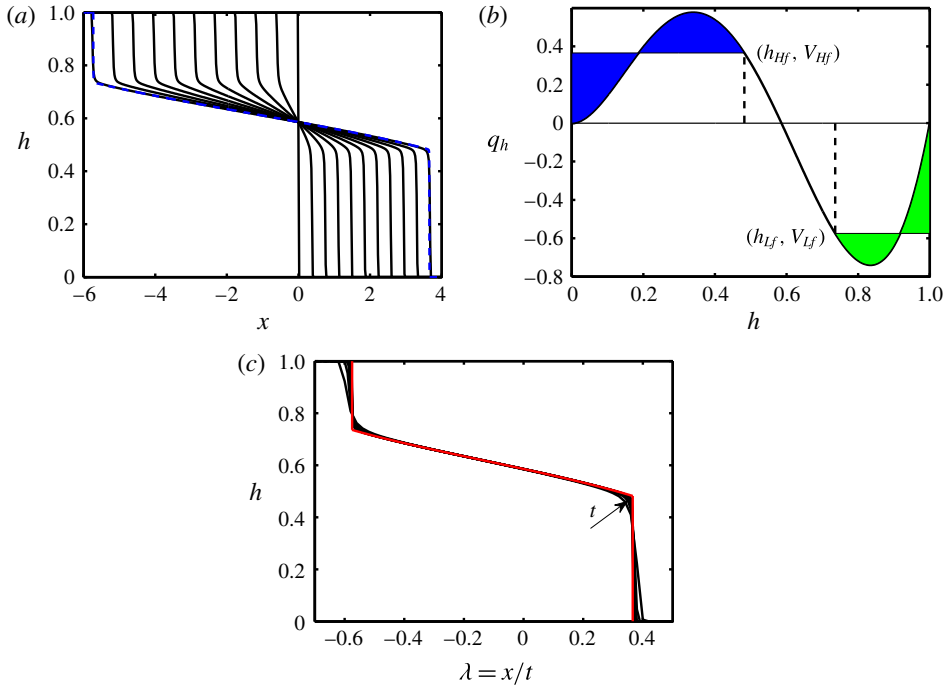
FIGURE 3. (Colour online) (*a*) Evolution of the interface height, h, with time, $t = [0, 1, 2, \ldots, 10]$, in exchange flow of two iso-viscous fluids ($\kappa = 1$) at $Re = 20$. Other parameters used are $\phi_0 = r_p = \xi = 0$. The blue dashed line shows the solution at $t = 10$ for $dx = 0.002$, which is almost indistinguishable from that of $dx = 0.02$. (*b*) Dependence of the derivative of the flux function, q_h, on h for the same parameters as in (*a*). The equal-area rules (5.4) and (5.5) can successfully predict the heavy and light front heights, $h_{Hf} \approx 0.482$ and $h_{Lf} \approx 0.736$, as well as velocities, $V_{Hf} \approx 0.366$ and $V_{Lf} \approx -0.575$. (*c*) Collapse of the interface height profiles using similarity parameter, $\lambda = x/t$. The red line shows the similarity solution obtained from (5.6).

Taghavi *et al.* (2009), the front heights, h_{Hf} and h_{Lf}, and speeds, λ_{Hf} $(= V_{Hf})$ and λ_{Lf} $(= V_{Lf})$, are determined from the equal-area rule

$$q(h_{Hf}) = h_{Hf} q_h(h_{Hf}), \tag{5.4}$$

$$-q(h_{Lf}) = (1 - h_{Lf}) q_h(h_{Lf}). \tag{5.5}$$

Figure 3(*b*) depicts the implementation of the equal-area rule for the example shown in figure 3(*a*). It is found that $h_{Hf} \approx 0.482$, $h_{Lf} \approx 0.736$, $V_{Hf} \approx 0.366$ and $V_{Lf} \approx -0.575$. The compound similarity solution for the flow shown in figure 3(*a*) is finally obtained as

$$h = \begin{cases} 1, & \lambda < -0.575, \\ -10(h^3 - 5h^2 + 6h - 2)h^2, & -0.575 \leqslant \lambda \leqslant 0.366, \\ 0, & \lambda > 0.366. \end{cases} \tag{5.6}$$

The analytical solution (5.6) and computed interface profiles at long time are shown in figure 3(*c*). The long-time behaviour is defined where there are no noticeable changes
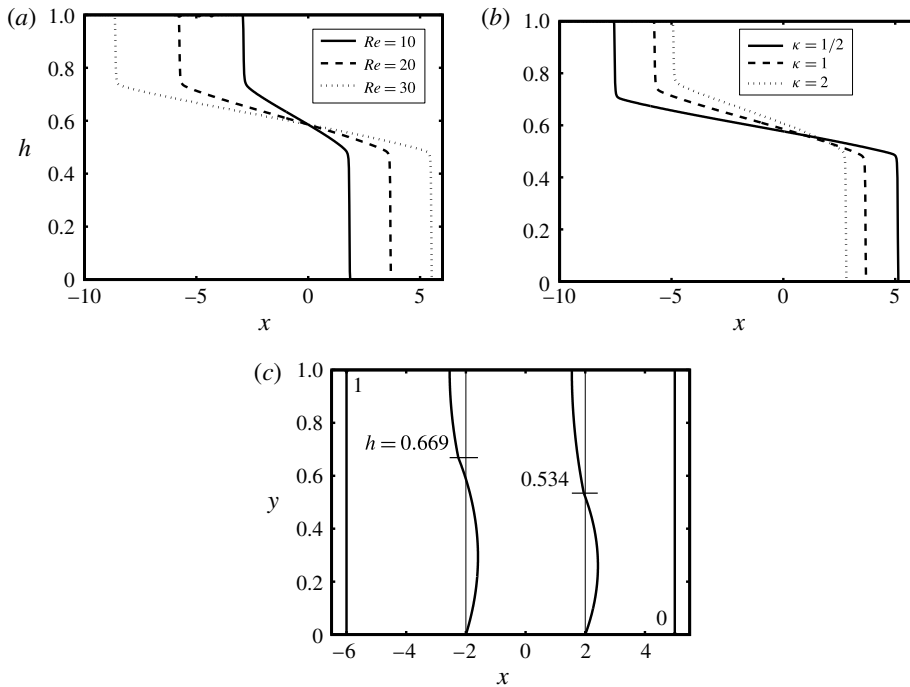
FIGURE 4. Comparison of the interface height, h, at $t = 10$ for (a) $\kappa = 1$ at different values of Re, and (b) $Re = 20$ at different values of κ. Other parameters used are $\phi_0 = r_p = \xi = 0$. (c) Streamwise velocity profile, u, plotted at locations $x = -6, -2, 2, 5$ corresponding to different interface heights, $h = 1, 0.669, 0.534, 0$, for the $\kappa = 2$ case in panel (b).

of the interface height behaviour with time, t. For instance, in figure 3(a), it can be seen that, as time progresses, the interface height front approaches the value of 0.482, i.e. the layers steadily interpenetrate into one another within a traceable path. The very close agreement found between the analytical solution (5.6) and the computation in figure 3(c) verifies the effectiveness of the similarity-solution approach.

Figure 4(a) compares the interface profiles at long time ($t = 10$) for $\kappa = 1$ and different values of Re. As observed, the interpenetration of the heavy and light layers is enhanced with Re. Larger Re can be interpreted as a higher density difference between the two fluids, which acts to intensify the exchange flow. Although the frontal speeds change with Re, the front heights remain unaffected. The effect of a viscosity contrast between the two fluids, κ, is shown in figure 4(b). It is evident that, at lower κ values (less viscous light fluid), the degree of interpenetration of the layers is higher, which is in agreement with the findings of Taghavi *et al.* (2009) and Matson & Hogg (2012) for slumping flows. Keeping $Re = \hat{\rho}_H(\phi_0)\hat{V}_t(2\hat{D})/\hat{\mu}_H(\phi_0)$ constant with more viscous heavy fluid (low κ) requires larger $\hat{V}_t$ or driving buoyancy force, which acts to expand the extent of the exchange zone (figure 4b). Unlike figure 4(a) shown for different values of Re, the front height does change with κ. It is insightful at this stage to look into the streamwise velocity profiles of a typical simulation. Figure 4(c) shows computed velocity profiles using (3.15) and (3.16) at different locations, $x = -6, -2, 2, 5$, for the $\kappa = 2$ case in figure 4(b). The calculated interface heights at the given x locations are, respectively, $h = 1, 0.669, 0.534, 0$. The velocity profile is perfectly
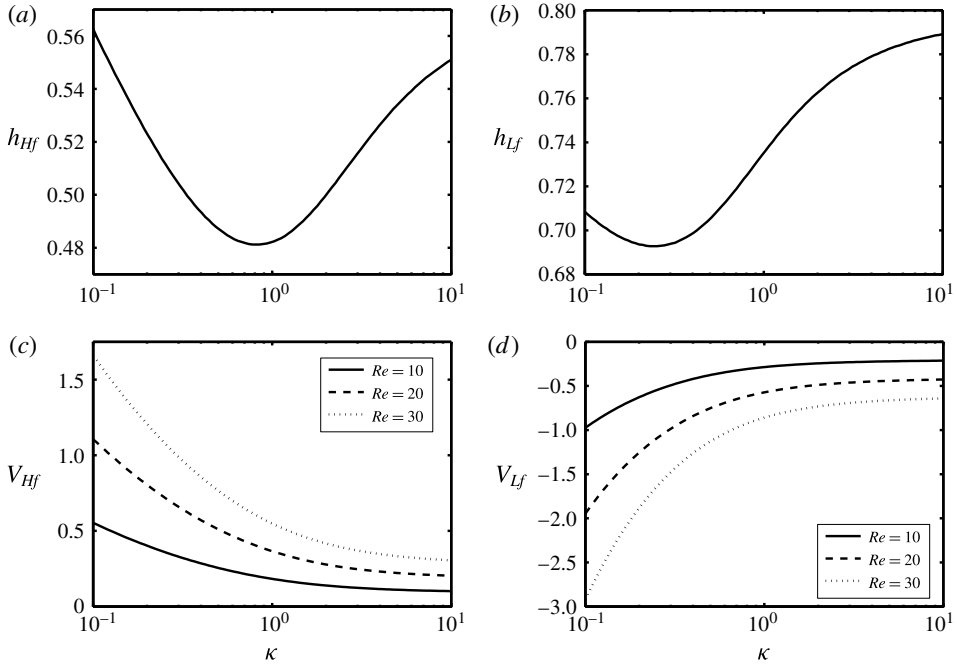
FIGURE 5. Variation of (*a*) heavy front height, h_{Hf}, and (*b*) light front height, h_{Lf}, versus κ for $\phi_0 = r_p = \xi = 0$ and all values of $Re > 0$. Panels (*c*) and (*d*) show the corresponding frontal velocities, V_{Hf} and V_{Lf}, of (*a*) and (*b*), respectively, at different values of Re.

zero at duct cross-sections that are full of heavy ($h = 1$) and light ($h = 0$) layers. The validity of the no-slip and no-stress conditions (3.11) and (3.12) at the wall ($y = 0$) and the duct centre ($y = 1$), respectively, is apparent. Since $\kappa = 2$ corresponds to a less viscous heavy fluid, we note a slightly larger gradient of velocity within this layer ($h = 0.669$ and 0.534 cases in figure 4*c*), which ensures homogeneity of shear stress across the interface; see condition (3.13).

The variation of the height and speed of heavy and light fronts at long time with κ and Re is shown in figure 5 using the equal-area rule. Figure 5(*a*,*b*) demonstrates the variation of h_{Hf} and h_{Lf}, respectively, over a wide range of κ. As predicted in figure 4(*a*), the heights of heavy and light fronts will not change with the Reynolds number. Therefore, the curves for all values of Re overlay in figure 5(*a*,*b*). The h_{Hf} value reaches a minimum at $\kappa \approx 0.8$, while the minimum h_{LF} value appears at a smaller viscosity contrast ($\kappa \approx 0.2$). Although h_{Hf} and h_{Lf} change non-monotonically with viscosity ratio, the variation of V_{Hf} and V_{Lf} with κ is monotonic, as shown in figure 5(*c*,*d*). Also note that, unlike the frontal height, the frontal speeds clearly depend on Re (speeds increasing with Re). The absolute values of V_{Hf} and V_{Lf} decrease with an increase in κ, as also revealed in figure 4(*b*).

5.2. *Particle-laden flows* ($\phi_0 > 0$)

We now examine particle-laden flows. Solving the governing system of PDEs (3.18) and (3.19) numerically when $\phi_0 \neq 0$, is more challenging, since an extremely small mesh size ($\mathrm{d}x \approx 2 \times 10^{-7}$) is required to fully capture the underlying effects of the flow (Cook *et al.* 2008). Figure 6(*a*) shows the evolution of the interface height profile,
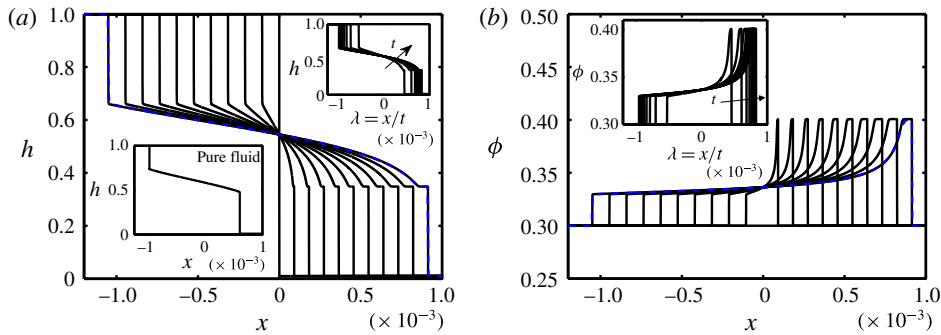
FIGURE 6. (Colour online) Evolution of the (*a*) interface height, h, and (*b*) particle volume fraction, ϕ, profiles with time, $t = [0, 0.01, 0.02, \ldots, 0.1]$. The parameters used are $\phi_0 = 0.3$, $Re = 0.1$, $\kappa = 1$, $r_p = 0.06$, $\xi = 1.9$ and $\eta = 1.25$. The blue dashed lines show the solution at $t = 0.1$ for $\mathrm{d}x = 2 \times 10^{-6}$, which is almost indistinguishable from that of $\mathrm{d}x = 2 \times 10^{-7}$. The lower left inset in (*a*) shows the corresponding interface profile in the pure fluid case obtained for the same Re and m values. The upper right inset in (*a*) and the one in (*b*) show the collapse of the profiles using the self-similarity parameter, $\lambda = x/t$.

h, at times $t = [0, 0.01, 0.02, \ldots, 0.1]$ for $\phi_0 = 0.3$, $Re = 0.1$ and $\kappa = 1$. The other parameters are chosen close to those in the experiments of Zhou *et al.* (2005) ($r_p = 0.06$, $\xi = 1.9$ and $\eta = 1.25$). The particle volume fraction value mostly chosen in our study ($\phi_0 = 0.3$) is selected such that a comparison with the results of Zhou *et al.* (2005) and Cook *et al.* (2008) can be made feasible. Understanding the suspension behaviour in the dense granular limit, $\phi_0 \to \phi_j$ (Lyon & Leal 1998), requires further study, which is outside the scope of the current paper. Note that the viscosity function (3.4) becomes singular as $\phi_0 \to \phi_j$. In the case of particle-laden flows, a zero precursor film thickness introduces a singularity into the solution, as laid out by Cook *et al.* (2008). To overcome such a singularity, we have used a small value of $b = 0.01$ in this paper unless otherwise stated; see also the experiments of Zhou *et al.* (2005) and the computations of Cook *et al.* (2008). The small choice of $t = 0.1$ for the case of figure 6 is due to the limited access to computational resources for carrying out these simulations. Nevertheless, even this small interval is enough to extrapolate the long-time behaviour of the flow, thanks to the self-similarity characteristic of the solutions. The top insets in figure 6(*a*,*b*) show the collapse of profiles using $\lambda = x/t$ with a small residual dependence on time that is comparable to that found by Taghavi *et al.* (2009) and Hasnain & Alba (2017) for displacement flows. Owing to the complex interface shape, the Rankine–Hugoniot similarity conditions of Zhou *et al.* (2005) may not be directly applied to the particle-laden exchange flows in confined geometry. The computed solution mesh independence is successfully confirmed in figure 6(*a*) for two different values of $\mathrm{d}x$.

In order to fully understand the effect of particle addition to exchange flows, we have added interface height profiles corresponding to the pure fluids as insets to the particle-laden figure results; see figures 6–13. The Reynolds number, Re, and mixture viscosity ratio, $m = m(\phi_0, \kappa)$, are kept the same in associated pure fluid and particle-laden cases. Upon comparing figure 6(*a*) to pure fluid results shown in the lower left inset, two important conclusions may be drawn. (1) The interface height profile in the presence of solid particles exhibits a plateau in the vicinity of the heavy

layer front ($h \approx 0.348$ and $\phi \approx 0.400$ as steady long-time behaviour). Such a plateau is reminiscent of the capillary ridge in the simulations of Hasnain & Alba (2017) but is formed under a completely different mechanism, namely the presence of solid particles. (2) The stretched interface between the heavy and light fronts also is more curved in the particle-laden case compared to the pure fluid. In order to understand these differences, we need to look at the volume fraction profiles, ϕ, as shown in figure 6(*b*). As is interestingly evident, there are jumps in ϕ along the duct length, *x*. In particular, there is an increase in ϕ close to the light layer front followed by a stronger jump in the vicinity of the heavy layer front. This pattern is different from that reported experimentally and theoretically by Zhou *et al.* (2005) for free-surface film flows. Owing to the lock exchange configuration and geometry confinement, we witness a two-step increase in ϕ close to the heavy and light layers instead of the one observed in the vicinity of the heavy front in the case of Zhou *et al.* (2005). The curvature of the interface height in the particle-laden case is then justified by the fact that the viscosity of the heavy solution is continuously changing along the streamwise direction through ϕ in (3.4), in turn modifying the dynamics of the exchange flow (see also figure 4*b*).

It has been hypothesized by Zhou *et al.* (2005) that the accumulation of particles close to the frontal region of the flow (e.g. in figure 6*b*) is due to the different transport rates of fluid and solid shown mathematically in (3.23) and (3.24). See also Auzerais, Jackson & Russel (1988) for similar shock formation effects in sedimentation problems. One question that might arise here is whether particle accumulation at the front can grow to an extent that causes pinch-off. In fact, by looking closely into the experiments of Zhou *et al.* (2005), Grunewald *et al.* (2010), Mata & Bertozzi (2011), Murisic *et al.* (2011, 2013), Mavromoustaki & Bertozzi (2014), Wang *et al.* (2015) and Wong & Bertozzi (2016) for particle-laden film flow down an incline, there is no evidence that such accumulation may lead to pinch-off. Also note that our computational code fails when particle enrichment approaches the jamming limit ($\mu \to \infty$ as $\phi \to \phi_j$). The lubrication model assumption will also not be valid close to this limit. As can be seen, in all presented simulations, the computed ϕ values are well below this jamming limit. Owing to settling Stokes velocity of particles (negative buoyancy), the particles accumulate close to the front. However, this accumulation does not grow unboundedly because at the same time the properties of the mixture, such as density (3.3) and viscosity (3.4), are also changing as a result of enrichment, eventually taking the frontal flow dynamics to a balanced state.

The effect of the precursor film thickness, *b*, is investigated in figure 7, keeping the rest of the controlling parameters the same as in figure 6. Figure 7(*a*) shows that, even though the shape of the light layer front remains unchanged, the one for the heavy layer is significantly affected by *b*; also compare against the inset representing the pure fluid case. The height of the heavy layer front and its extent increase with *b*. An increase in the frontal height is accompanied by a decrease in the level of particle enrichment, as evident in figure 7(*b*). For small values of *b*, the particle-rich zone grows to an extent that might cause singularity in the solution ($\mu_H \to \infty$ as $\phi \to \phi_j$). This observation is in complete agreement with the findings of Zhou *et al.* (2005) and Cook *et al.* (2008) for free-surface film flows. In fact, they mention that this complex frontal shock behaviour may not be entirely captured by a first-order lubrication model. A singular shock behaviour in our model may also be observed at high initial volume fractions. As discussed by Cook *et al.* (2008), using the Buscall settling function instead of Richardson–Zaki may alleviate such a singularity, which requires further study. Figures 8(*a*) and 8(*b*) compare the profiles of the interface
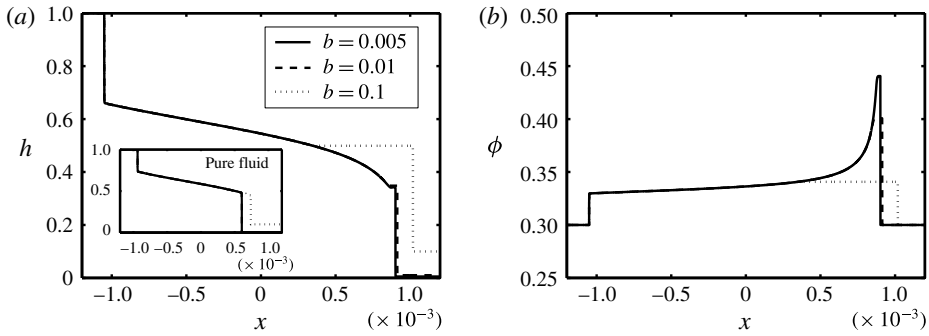
FIGURE 7. Change in (*a*) interface height, *h*, and (*b*) particle volume fraction, ϕ, with *x* at $t = 0.1$ and various values of the precursor film thickness, *b*. Other parameters used are $\phi_0 = 0.3$, $Re = 0.1$, $\kappa = 1$, $r_p = 0.06$, $\xi = 1.9$ and $\eta = 1.25$. The inset in (*a*) shows the corresponding interface profiles to the pure fluid case obtained for the same *Re* and *m* values.
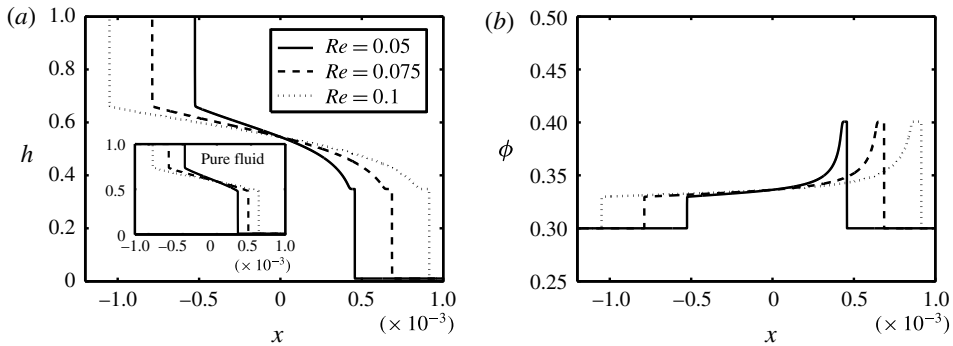

FIGURE 8. Change in (*a*) interface height, *h*, and (*b*) particle volume fraction, ϕ, with *x* at $t = 0.1$ and various values of the Reynolds number, *Re*. Other parameters used are $\phi_0 = 0.3$, $\kappa = 1$, $r_p = 0.06$, $\xi = 1.9$ and $\eta = 1.25$. The inset in (*a*) shows the corresponding interface profiles to the pure fluid case obtained for the same *Re* and *m* values.

height, *h*, and particle volume fraction, ϕ, respectively, at various values of the Reynolds number, *Re*. In compliance with our observation in figure 8(*a*) inset for pure fluids, the interpenetration rate of the heavy and light layers similarly increases with *Re*. Moreover, the heights of the heavy and light fronts remain the same while changing *Re*. The constancy in advancing front heights is accompanied by uniform increase in volume fraction of particles; see figure 8(*b*).

The initial volume fraction of particles, ϕ_0, plays an important role in the dynamics of the flow, as it controls both the density (3.3) and viscosity (3.4) of the heavy mixture. Keeping all the other parameters constant, the dependence of the interface height, *h*, and volume fraction of particles, ϕ, on ϕ_0 is investigated in figures 9(*a*) and 9(*b*) respectively. The extent of the exchange flow is decreased with ϕ_0 as shown in figure 9(*a*). While the density of the heavy mixture, $\hat{\rho}_H$, increases with ϕ_0 (larger driving force), its viscosity, $\hat{\mu}_H$, also increases, which results in an overall slowdown of the flow. The frontal heights of the heavy and light layers are shown to minutely increase with ϕ_0. The corresponding profiles to the pure fluid case are shown in the inset of figure 9(*a*). An increase in ϕ_0 results in a decrease in the effective mixture viscosity ratio, *m*, which can mildly extend the exchange zone between the two fluids
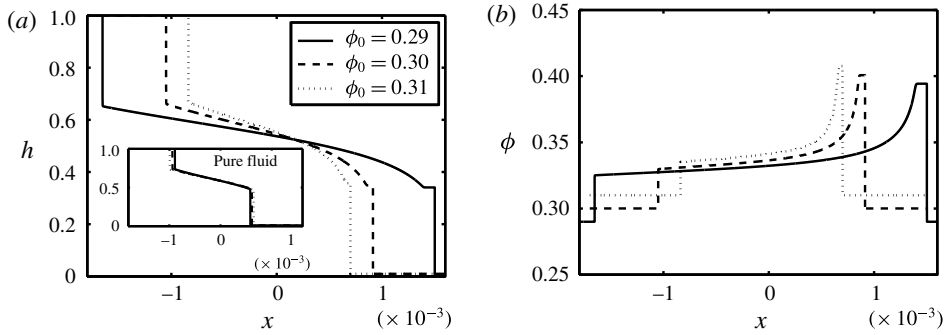
FIGURE 9. Change in (*a*) interface height, *h*, and (*b*) particle volume fraction, ϕ, with *x* at $t = 0.1$ and various values of the initial particle volume fraction, ϕ_0. Other parameters used are $Re = 0.1$, $\kappa = 1$, $r_p = 0.06$, $\xi = 1.9$ and $\eta = 1.25$. The inset in (*a*) shows the corresponding interface profiles to the pure fluid case obtained for the same *Re* and *m* values.
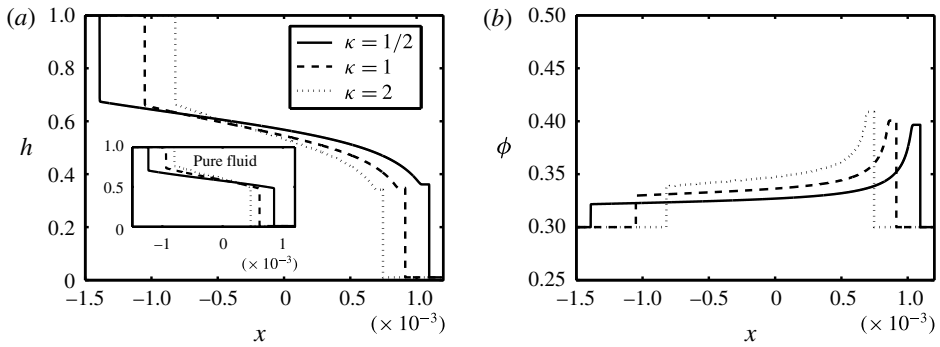

FIGURE 10. Change in (*a*) interface height, *h*, and (*b*) particle volume fraction, ϕ, with *x* at $t = 0.1$ and various values of the light-to-carrying-fluid viscosity ratio, κ. Other parameters used are $\phi_0 = 0.3$, $Re = 0.1$, $r_p = 0.06$, $\xi = 1.9$ and $\eta = 1.25$. The inset in (*a*) shows the corresponding interface profiles to the pure fluid case obtained for the same *Re* and *m* values.

observed from the inset of figure 9(*a*); see also figure 4(*b*). Particle enrichment close to the heavy and light fronts is consistently observed over a range of ϕ_0 (figure 9*b*). However, the relative rise in particle concentration seems to be slightly less for higher ϕ_0; compare, for example, the $\phi_0 = 0.29$ and 0.31 curves in figure 9(*b*). The general features of the flow, such as interface height curvature as well as particle enrichment close to the heavy front, for other values of ϕ_0, e.g. in the dilute range $\phi_0 = 0.01$ (Segre & Silberberg 1961), are similar to those obtained for $\phi_0 \approx 0.3$. Results are not presented here for brevity.

The increase in light-to-carrying-fluid viscosity ratio, κ, tends to contract the exchange zone between the two fluids, as shown in figure 10(*a*). Comparing this to the results for pure exchange flows shown as the inset, we infer that the height of the heavy front in the particle-laden case slightly decreases with κ, which is complemented by a growth in the volume fraction of particles, ϕ (figure 10*b*). Note that in the case of free-surface film flow of Zhou *et al.* (2005) and Cook *et al.* (2008), an increase (decrease) in the frontal height is only achieved by an increase (decrease) in local particle volume fraction. However, in a confined geometry, various
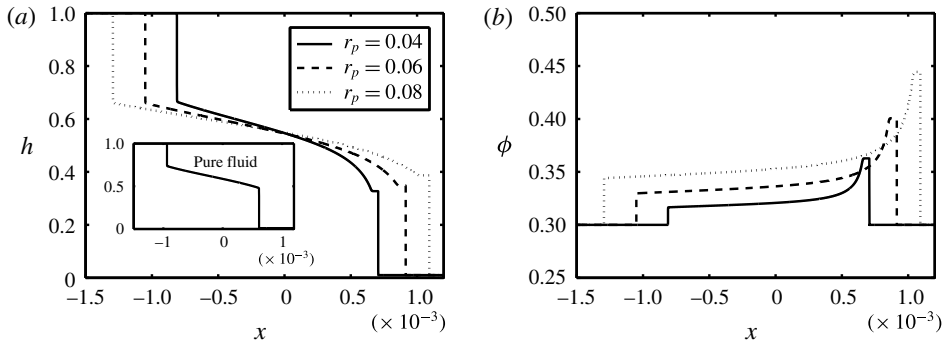
FIGURE 11. Change in (*a*) interface height, *h*, and (*b*) particle volume fraction, ϕ, with x at $t = 0.1$ and various values of the particle-radius-to-half-duct-width ratio, r_p. Other parameters used are $\phi_0 = 0.3$, $Re = 0.1$, $\kappa = 1$, $\xi = 1.9$ and $\eta = 1.25$. The inset in (*a*) shows the corresponding interface profile to the pure fluid case obtained for the same Re and m values.

intricate scenarios might happen at the front; for example, the frontal height might decrease while particle volume fraction increases (figure 10) and *vice versa* (figure 7). Let us physically explain the increase of ϕ with κ observed in figure 10(*b*). Large κ corresponds to small $\hat{\mu}_{f,H}$. Considering the definition, the dimensionless Stokes velocity, $u_0 = 2\hat{a}^2(\hat{\rho}_p - \hat{\rho}_{f,H})\hat{g}/(9\hat{V}_t\hat{\mu}_{f,H})$, is increased as $\hat{\mu}_{f,H}$ is decreased. Larger u_0 increases particle slip velocity in the G flux function (3.24), which will consequently result in stronger accumulation of particles, as shown in figure 10(*b*). In the case of Zhou *et al.* (2005) and Cook *et al.* (2008), the flow dynamics is basically governed by particles settling within a single carrying fluid plus the no-stress condition imposed at the free surface. However, in the current channel flow case, we have not only the effect of the particles' slip velocity but also the interaction of the carrying and light fluids at the interface captured via the stress homogeneity condition (3.13). Such a combination gives rise to complex patterns observed in the channel geometry as opposed to the free-surface geometry.

Investigating the effect of the relative size of particles, r_p, can provide more insight into the dynamics of the exchange flow in question. Figure 11 shows the interface height and particle volume fraction profiles for the same parameters as in figure 6 except r_p. An increase in the size of particles consistently increases the height of the heavy front (figure 11*a*) and local volume fraction (figure 11*b*). Note a similar increase in ϕ close to the light fluid front as well as the heavy one. As is evident in figure 11(*a*), the interface between the two fluids has been extended with r_p. Let us have a fundamental look into this effect. The increase in $r_p = \hat{a}/\hat{D}$ can be interpreted as either an increase in particle radius, $\hat{a}$, or a decrease in half the duct width, $\hat{D}$. If we supposedly consider the latter, then from the Reynolds-number expression given in table 2, *Re* should therefore decrease. Increasing r_p while keeping *Re* the same in figure 11 requires, for instance, a decrease in the heavy mixture viscosity, $\hat{\mu}_H(\phi_0)$, which is achievable by decreasing the carrying fluid viscosity, $\hat{\mu}_{f,H}$; see § 2. In order to keep $\kappa = \hat{\mu}_L/\hat{\mu}_{f,H}$ the same in figure 11, $\hat{\mu}_L$ will also be decreased. A decrease in the carrying and light fluids viscosity, on the other hand, acts to ease the advancement of the exchange flow as confirmed in figure 11(*a*). The effect of r_p is also directly reflected in the particles' dimensionless Stokes velocity, $u_0 = (\xi - 1)\psi\kappa Re(1 + \psi)r_p^2/(9m\eta(1 - \psi))$, which feeds into the flux function G
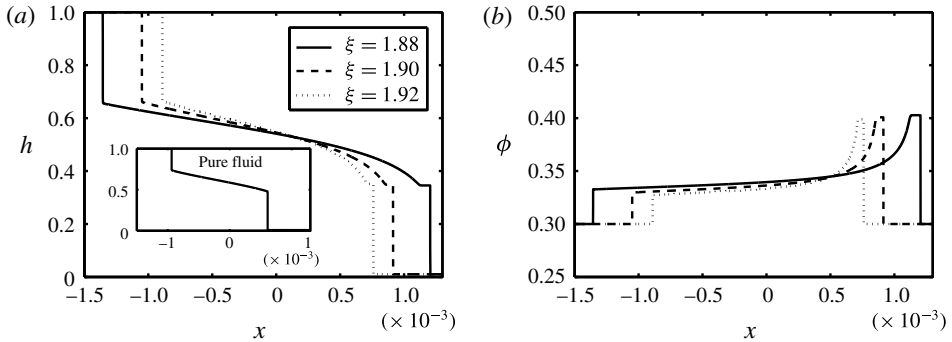
FIGURE 12. Change in (*a*) interface height, *h*, and (*b*) particle volume fraction, ϕ, with *x* at $t = 0.1$ and various values of the particle-to-carrying-fluid density ratio, ξ. Other parameters used are $\phi_0 = 0.3$, $Re = 0.1$, $\kappa = 1$, $r_p = 0.06$ and $\eta = 1.25$. The inset in (*a*) shows the corresponding interface profile to the pure fluid case obtained for the same *Re* and *m* values.

in (3.24). An increase in r_p enhances the settling speed of the particles, which in turn causes accumulation of particles close to the advancing frontal regions.

Another factor that can potentially enhance the Stokes settling velocity of the particles is the particle-to-carrying-fluid density ratio, ξ; see figure 12. As opposed to r_p, an increase in ξ reduces the interpenetration rate of the heavy and light layers; see figure 12(*a*). At first glance, this effect seems rather counterintuitive since an increase in ξ indicates heavier particles, which should, in turn, increase the buoyant driving force of the flow. However, similar to the rationale presented for figure 11, we need to consider the fact that the depicted profiles are obtained for constant Reynolds number, $Re = \hat{\rho}_H(\phi_0)\hat{V}_t(2\hat{D})/\hat{\mu}_H(\phi_0)$. From §2, we learnt that *Re* depends on $\hat{V}_t$, which, by itself, decreases with ψ since $\hat{V}_t = \sqrt{(1 - \psi)\hat{g}\hat{D}/(1 + \psi)}$. The parameter $\psi = \eta/(1 + (\xi - 1)\phi_0)$ is inversely related to ξ. Therefore, increasing ξ (thus $\hat{V}_t$) meanwhile keeping *Re* constant may be deduced as an increase in $\hat{\mu}_H(\phi_0) = \hat{\mu}_{f,H}(1 - \phi_0/\phi_j)^{-2}$ or $\hat{\mu}_{f,H}$. Since $\kappa = \hat{\mu}_L/\hat{\mu}_{f,H} = 1$, we shall also have $\hat{\mu}_L$ increasing. As a result, flow deceleration will occur for high ξ, which is correspondingly confirmed in figure 12(*a*). Furthermore, the increase in volume fraction of particles for high ξ (settling in high-viscosity medium) is slightly less than, but still comparable to, that of low ξ due to the higher density of solids in the former (figure 12*b*).

Finally, the variations of the interface height, *h*, and particle volume fraction, ϕ, versus the light-to-carrying-fluid density ratio, η, are examined in figures 13(*a*) and 13(*b*), respectively. Even though the presented η values are all larger than unity, i.e. light fluid denser than carrying fluid, the overall density of the suspension mixture is always larger than the light pure fluid ($\psi < 1$). Note that the interpenetration extent of the mixtures has increased with η (figure 13*a*). Similar to figure 12, this effect also appears counterintuitive at first. This is because an increase in η means a denser light fluid in the lower section of the duct compared to the carrying fluid at the top, i.e. a decrease in the effective density difference between the heavy and light mixtures. Increasing η meanwhile keeping *Re* the same in figure 13(*a*) requires, for instance, a reduction in the viscosity of the involved fluids ($Re \propto \hat{\rho}_H(\phi_0)/\hat{\mu}_H(\phi_0)$), which consequently enhances flow acceleration. The front height on the heavy side
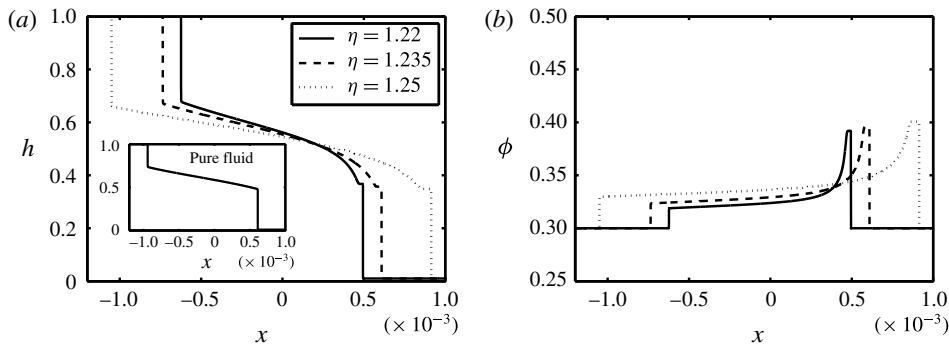
FIGURE 13. Change in (*a*) interface height, *h*, and (*b*) particle volume fraction, ϕ, with *x* at $t = 0.1$ and various values of the light-to-carrying-fluid density ratio, η. Other parameters used are $\phi_0 = 0.3$, $Re = 0.1$, $\kappa = 1$, $r_p = 0.06$ and $\xi = 1.9$. The inset in (*a*) shows the corresponding interface profile to the pure fluid case obtained for the same *Re* and *m* values.

slightly decreases with an increase in η. As η increases (while keeping *Re* constant), the mixture's viscosity decreases, facilitating particle settling and thus enrichment in volume fraction, ϕ, close to the fronts (figure 13*b*). Since r_p, ξ and η do not affect the mixture's viscosity ratio, $m = \kappa(1 - \phi_0/\phi_j)^2$, the shape of the interface height obtained in the pure fluid limit remains unchanged with these parameters; see insets shown in figures 11(*a*)–13(*a*).

6. Conclusions

Buoyancy-driven exchange flow of two mixtures in a vertical duct (2D channel as well as pipe) is investigated theoretically. The light mixture is always assumed to be a pure fluid, whereas the heavy mixture can be either pure or particle-laden. Assuming a small aspect ratio for the duct, δ, a lubrication model is developed. The methodology of Zhou *et al.* (2005) for free-surface particle-laden film flows is employed and extended to a lock exchange system in a confined geometry under the Boussinesq limit. The derived model takes the simple form of the classical Riemann problem. A robust TVD finite difference scheme is implemented to solve the model PDEs numerically. The solutions suggest self-similar interface shapes over time. In the limit of small aspect ratio ($\delta \ll 1$) and assuming a jamming volume fraction of $\phi_j \approx 0.67$, six dimensionless parameters govern the flow, namely, particle-radius-to-half-duct-width ratio, r_p, particle-to-carrying-fluid density ratio, ξ, light-to-carrying-fluid density ratio, η, light-to-carrying-fluid viscosity ratio, κ, initial volume fraction of particles, ϕ_0, and the Reynolds number, *Re*. Owing to the choice of scaling, the dynamics of the flow for pure fluids ($\phi_0 = r_p = \xi = 0$) is governed only by κ and *Re*. The physical effect of these parameters on the dynamics of the flow has been quantified through a systematic approach. It is observed that the interpenetration rate of the heavy and light layers increases with *Re* and decreases with κ. The heights of the heavy and light fronts change with κ but remain unchanged with *Re*. The dynamics of the exchange flow becomes entirely different in the presence of solid particles compared to pure fluids. Primarily, the interface profiles are more curved in the former with respect to the latter due to change of viscosity along the duct. Novel particle-rich zones inside the suspension are further discovered in the vicinity of the advancing heavy and light fronts. The particle enrichment at the fronts is associated with different transport rates

of fluid and solid due to the Stokes settling velocity of the particles. It is also revealed that geometry confinement plays a significant role in exchange flow dynamics such as formation of interfacial patterns and particle-enrichment behaviour. Whereas, in the unconfined geometry, particle enrichment was shown to be accompanied by an increase in the interface height profile, in a confined duct, either an increase or a decrease in height is possible depending on the controlling parameters of the flow. The level of particle enrichment remains the same with Re, is enhanced by κ, r_p and η, and is slightly reduced with ϕ_0 and ξ. The stretched interface between the heavy and light fronts grows with r_p, η and Re, but shrinks with ϕ_0, κ and ξ. The model can be easily extended to include interfacial tension effects; see Hasnain & Alba (2017) for similar implementation in the case of pure fluids.

Acknowledgements

Appendix A. Shear-induced migration effects

Migration of particles induced by shear is in fact an important effect widely observed in particle-laden flows. Our methodology follows the approach of Zhou *et al.* (2005) for gravity-driven suspension film flow down an incline, which neglects the shear-induced migration effect (Schaflinger, Acrivos & Zhang 1990; Acrivos, Fan & Mauri 1994). In this appendix we would like to verify the conditions under which such an assumption is valid. The particle transport equation for particle-laden film flows is given by Murisic *et al.* (2013) and Wong & Bertozzi (2016) as

$$\phi_{\hat{t}} + \hat{u}\phi_{\hat{x}} + \hat{v}\phi_{\hat{y}} = -\hat{\boldsymbol{J}}_{\hat{x},\hat{x}} - \hat{\boldsymbol{J}}_{\hat{y},\hat{y}}. \tag{A 1}$$

Here, $\hat{\boldsymbol{J}}$ is the particle flux due to settling and migration,

$$\hat{\boldsymbol{J}} = \hat{\boldsymbol{J}}_{settling} + \hat{\boldsymbol{J}}_{migration}. \tag{A 2}$$

The settling and migration flux components can be expressed as the following (Murisic *et al.* 2013; Wong & Bertozzi 2016):

$$\hat{\boldsymbol{J}}_{settling} = \frac{2\hat{a}^2 \hat{g}(\hat{\rho}_p - \hat{\rho}_{f,H})}{9\hat{\mu}_{f,H}}(1 - \phi)\phi, \tag{A 3}$$

$$\hat{\boldsymbol{J}}_{migration} = -\frac{\hat{a}^2 \hat{V}_t}{\hat{D}^2}\left[K_c\phi\boldsymbol{\nabla}(\phi u_y) + \frac{K_v\phi^2 u_y}{\mu_H}\boldsymbol{\nabla}\mu_H\right]. \tag{A 4}$$

The constants $K_c \approx 0.41$ and $K_v \approx 0.62$ correspond to shear-induced particle flux due to gradients in the particle volume fraction and effective viscosity of the suspension, which are determined empirically (Phillips *et al.* 1992; Wong & Bertozzi 2016). From the velocity expression (3.15), it can be found that $u_y \sim Re$; see also appendix C for the coefficients. Therefore, the largest flux component due to shear-induced migration in (A 4) is of order $K_v\hat{a}^2 \hat{V}_t Re/\hat{D}^2$, whereas that of settling is the coefficient of the $(1 - \phi)\phi$ term in (A 3), i.e. $2\hat{a}^2 \hat{g}(\hat{\rho}_p - \hat{\rho}_{f,H})/(9\hat{\mu}_{f,H})$. Note that the rest of the terms in
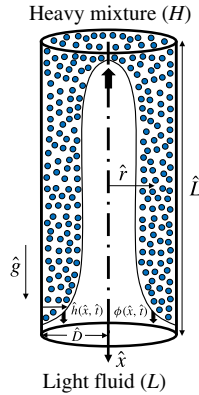
FIGURE 14. (Colour online) Schematic of axisymmetric particle-laden exchange flow in a vertical pipe.

(A 3) and (A 4) being multiplied by these coefficients are $O(1)$ since they are made dimensionless. By requiring that the settling effects overcome those of migration ($\hat{\boldsymbol{J}}_{settling} \gg \hat{\boldsymbol{J}}_{migration}$), the following condition is finally obtained:

$$\frac{9K_v\eta(1 - \phi_0/\phi_j)^2}{\psi(\xi - 1)}\frac{(1 - \psi)}{(1 + \psi)} \ll 1. \tag{A 5}$$

Note that the $(1 - \psi)/(1 + \psi)$ term in (A 5) is nothing other than the effective Atwood number, $At = (\hat{\rho}_H(\phi_0) - \hat{\rho}_L)/(\hat{\rho}_H(\phi_0) + \hat{\rho}_L)$. In other words, the Boussinesq limit ($At \ll 1$), discussed by Taghavi *et al.* (2012*b*), ensures that the shear-induced migration effects are negligible in front of settling. Note that the rest of the terms in (A 5) are approximately $O(1)$. From a fundamental standpoint, the small Atwood number or density difference between the mixtures does not cause a strong countercurrent and shear in the flow, which would lead to migration. However, in the meantime, the particles would have the opportunity to settle due to their weight. The condition (A 5) is indeed valid in the simulations presented in this paper. For instance, for a typical set of parameters chosen in our study, e.g. in figure 6, the left-hand side term in the condition above is approximately 0.019, i.e. settling flux more than 50 times stronger than that of shear-induced migration.

Appendix B. Axisymmetric flow in pipe

Performing exchange flow experiments in a pipe geometry can be more feasible compared to the 2D channel geometry. Therefore, in this appendix the exchange flow model is extended to a practical pipe geometry; see figure 14. It is not difficult to show that in cylindrical coordinates the momentum equations (3.9) and (3.10) take the following forms:

$$0 = -P_{0,x} + \mu_H(\phi)(ru_r)_r/r, \quad 1 - h \leqslant r \leqslant 1, \tag{B 1}$$

$$0 = -P_{0,x} - (\rho_H(\phi) - \psi)Re/(1 - \psi) + m(ru_r)_r/r, \quad 0 \leqslant r \leqslant 1 - h. \tag{B 2}$$

Applying appropriate boundary and interfacial conditions, equations (B 1) and (B 2) can be integrated with respect to r in order to determine the streamwise velocity

closures in each layer. The flux function, $q = \hat{q}/(\pi \hat{D}^2 \hat{V}_t)$, as the flow rate within the heavy layer, can eventually be calculated as

$$q = 2 \int_{1-h}^{1} r u \, dr, \tag{B 3}$$

which is given below as a function of h, Re, m, μ_H, ρ_H and ψ:

$$
\begin{aligned}
q = {} & -(1/8)Re \, [-4\ln(1-h)\mu_H\psi - 104h^6 m\psi - 144h^5\mu_H\psi + 176h^5 m\psi \\
& - 80h^3 m\rho_H + 16h^2 m\rho_H + 164h^4 m\rho_H + 144h^5\mu_H\rho_H + 104h^6 m\rho_H \\
& + 80h^6\mu_H\psi + 92h^3\mu_H\rho_H - 30h^2\mu_H\rho_H + 4h\mu_H\rho_H - 4h^8 m\psi + 32h^7 m\psi \\
& + 4h^8 m\rho_H - 32h^7 m\rho_H - 24h^7\mu_H\psi + 24h^7\mu_H\rho_H + 3h^8\mu_H\psi - 3h^8\mu_H\rho_H \\
& + 280\ln(1-h)h^4\mu_H\rho_H - 208\ln(1-h)h^3 m\psi + 208\ln(1-h)h^3 m\rho_H \\
& + 224\ln(1-h)h^3\mu_H\psi - 224\ln(1-h)h^3\mu_H\rho_H - 112\ln(1-h)h^2\mu_H\psi \\
& + 112\ln(1-h)h^2\mu_H\rho_H + 32\ln(1-h)h\mu_H\psi - 32\ln(1-h)h\mu_H\rho_H \\
& + 88\ln(1-h)h^2 m\psi - 88\ln(1-h)h^2 m\rho_H - 16\ln(1-h)hm\psi \\
& + 16\ln(1-h)hm\rho_H + 4\ln(1-h)h^8 m\psi - 32\ln(1-h)h^7 m\psi \\
& - 4\ln(1-h)h^8 m\rho_H + 32\ln(1-h)h^7 m\rho_H - 4\ln(1-h)h^8\mu_H\psi \\
& + 32\ln(1-h)h^7\mu_H\psi + 4\ln(1-h)h^8\mu_H\rho_H - 32\ln(1-h)h^7\mu_H\rho_H \\
& + 112\ln(1-h)h^6 m\psi - 112\ln(1-h)h^6 m\rho_H - 112\ln(1-h)h^6\mu_H\psi \\
& + 112\ln(1-h)h^6\mu_H\rho_H - 224\ln(1-h)h^5 m\psi + 224\ln(1-h)h^5 m\rho_H \\
& + 224\ln(1-h)h^5\mu_H\psi - 224\ln(1-h)h^5\mu_H\rho_H + 276\ln(1-h)h^4 m\psi \\
& - 276\ln(1-h)h^4 m\rho_H - 280\ln(1-h)h^4\mu_H\psi - 92h^3\mu_H\psi - 164h^4 m\psi \\
& - 4h\mu_H\psi + 30h^2\mu_H\psi + 80h^3 m\psi - 16h^2 m\psi + 151h^4\mu_H\psi - 151h^4\mu_H\rho_H \\
& - 80h^6\mu_H\rho_H - 176h^5 m\rho_H + 4\ln(1-h)\mu_H\rho_H] / [\mu_H \, (h^4 m\psi - h^4\mu_H\psi \\
& - h^4 m + h^4\mu_H - 4h^3 m\psi + 4h^3\mu_H\psi + 4h^3 m - 4h^3\mu_H + 6h^2 m\psi - 6h^2\mu_H\psi \\
& - 6h^2 m + 6h^2\mu_H - 4hm\psi + 4h\mu_H\psi + 4hm - 4h\mu_H - \mu_H\psi + \mu_H)]. \tag{B 4}
\end{aligned}
$$

Similar to (3.21) and (3.22), the evolution equations for the interface height and particle volume fraction in cylindrical coordinates, respectively, read

$$H_t + F_x(H, \Theta) = 0, \tag{B 5}$$

$$\Theta_t + G_x(H, \Theta) = 0, \tag{B 6}$$

where $H = (1-h)^2$, $\Theta = \theta(1 - (1-h)^2)/h$ and

$$F(H, \Theta) = -q(H, \Theta), \tag{B 7}$$

$$G(H, \Theta) = -\frac{\Theta F(H, \Theta)}{1-H} + u_0 \Theta \left(1 - \frac{\Theta}{1-H}\right) f(H, \Theta) w(H). \tag{B 8}$$

Using exactly the same numerical scheme as the one explained in §4, the system of PDEs (B 5) and (B 6) can be solved to give evolution of H and Θ (thus h and ϕ) in space x and time t. Figures 15(a) and 15(b) show sample computed results in pipe geometry for the pure fluid ($\phi_0 = 0$) and suspension cases ($\phi_0 = 0.3$), respectively. Figure 15(a) compares the pipe interface profile with that of 2D channel shown earlier in figure 3(a). The effect of geometry on spreading of heavy and light layers is evident.
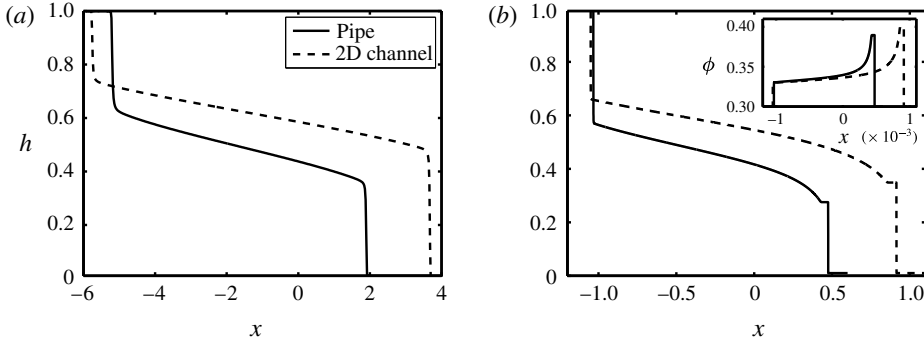
FIGURE 15. Comparison of the pipe interface height profile, h, for (*a*) pure fluid ($\phi_0 = 0$) and (*b*) particle-laden cases ($\phi_0 = 0.3$) against the results of the 2D channel presented earlier in figures 3 and 6, respectively. The inset in panel (*b*) depicts the corresponding profile of volume fraction, ϕ.

The computed heavy and light frontal shock heights ($h_{HF} \approx 0.36$ and $h_{LF} \approx 0.63$) were successfully compared to those obtained from an equal-area rule in a pipe (see also (5.4)–(5.5) and Taghavi *et al.* (2011)):

$$q(h_{Hf}) = (1 - (1 - h_{HF})^2)q_h(h_{Hf})/[2(1 - h_{HF})], \qquad (B\,9)$$

$$-q(h_{Lf}) = (1 - h_{LF})^2 q_h(h_{Lf})/[2(1 - h_{LF})]. \qquad (B\,10)$$

Figure 15(*b*) compares the pipe interface profile against that of a 2D channel shown earlier in figure 6 for the particle-laden case. The inset depicts the corresponding profile of volume fraction, ϕ. A similar particle enrichment effect to the 2D channel case is observed with only slight modification due to the geometric difference. Figure 15 suggests that the heavy and light frontal height, h, is larger in the case of a channel compared to the pipe. Moreover, the exchange flow overall advances more rapidly in the former.

Appendix C. Coefficients in velocity expressions (3.15) and (3.16) for 2D channel case

$$
\begin{aligned}
P_{0,x} = {}& -\big[(3h^3 m - 2h^3 \mu_H - 9h^2 m + 6h^2 \mu_H + 6hm - 6h\mu_H + 2\mu_H)\psi - 3h^3 m\rho_H \\
& + 2h^3 \mu_H \rho_H + 9h^2 m\rho_H - 6h^2 \mu_H \rho_H - 6hm\rho_H + 6h\mu_H \rho_H - 2\mu_H \rho_H\big]Re/ \\
& \big[2(\psi - 1)(h^3 m - h^3 \mu_H - 3h^2 m + 3h^2 \mu_H + 3hm - 3h\mu_H + \mu_H)\big], \qquad (C\,1)
\end{aligned}
$$

$$
\begin{aligned}
c_1 = {}& \big[(2h^3 m - 2h^3 \mu_H - 5h^2 m + 6h^2 \mu_H + 3hm - 6h\mu_H + 2\mu_H)\psi \\
& - 2h^3 m\rho_H + 2h^3 \mu_H \rho_H + 5h^2 m\rho_H - 6h^2 \mu_H \rho_H - 3hm\rho_H + 6h\mu_H \rho_H \\
& - 2\mu_H \rho_H\big]hRe/\big[2\mu_H\big((h^3 m - h^3 \mu_H - 3h^2 m + 3h^2 \mu_H + 3hm - 3h\mu_H + \mu_H)\psi \\
& - h^3 m + h^3 \mu_H + 3h^2 m - 3h^2 \mu_H - 3hm + 3h\mu_H - \mu_H)\big], \qquad (C\,2)
\end{aligned}
$$

$$c_2 = 0, \qquad (C\,3)$$

$$
\begin{aligned}
d_1 = {}& [(h - 3)\psi - h\rho_H + 3\rho_H]h^2 Re/ \\
& [2(\psi - 1)(h^3 m - h^3 \mu_H - 3h^2 m + 3h^2 \mu_H + 3hm - 3h\mu_H + \mu_H)], \qquad (C\,4)
\end{aligned}
$$

$$d_2 = \big[(h^3 m - h^3 \mu_H - h^2 m + h^2 \mu_H + 2\mu_H)\psi - h^3 m\rho_H + h^3 \mu_H \rho_H + h^2 m\rho_H$$
$$- h^2 \mu_H \rho_H - 2\mu_H \rho_H\big]h^2 Re/$$
$$\big[4\mu_H(\psi - 1)(h^3 m - h^3 \mu_H - 3h^2 m + 3h^2 \mu_H + 3hm - 3h\mu_H + \mu_H)\big]. \tag{C 5}$$

Appendix D. Flux function, q, in (3.17) for 2D channel case

$$q = \big[(3h^3 m - 4h^3 \mu_H - 6h^2 m + 12h^2 \mu_H + 3hm - 12h\mu_H + 4\mu_H)\psi - 3h^3 m\rho_H$$
$$+ 4h^3 \mu_H \rho_H + 6h^2 m\rho_H - 12h^2 \mu_H \rho_H - 3hm\rho_H + 12h\mu_H \rho_H - 4\mu_H \rho_H\big]h^3 Re/$$
$$\big[12\mu_H\big((h^3 m - h^3 \mu_H - 3h^2 m + 3h^2 \mu_H + 3hm - 3h\mu_H + \mu_H)\psi - h^3 m$$
$$+ h^3 \mu_H + 3h^2 m - 3h^2 \mu_H - 3hm + 3h\mu_H - \mu_H\big)\big]. \tag{D 1}$$

For pure fluids, $\phi_0 = 0$ and $\rho_H = \mu_H = 1$. Therefore, q is reduced to

$$q = \frac{(3h^3 m - 4h^3 - 6h^2 m + 12h^2 + 3hm - 12h + 4)h^3 Re}{12(h^3 m - h^3 - 3h^2 m + 3h^2 + 3hm - 3h + 1)}. \tag{D 2}$$

REFERENCES

ACRIVOS, A., FAN, X. & MAURI, R. 1994 On the measurement of the relative viscosity of suspensions. *J. Rheol.* **38** (5), 1285–1296.

ALBA, K., LAURE, P. & KHAYAT, R. E. 2011 Transient two-layer thin-film flow inside a channel. *Phys. Rev.* E **84**, 026320.

ALBA, K., TAGHAVI, S. M. & FRIGAARD, I. A. 2012 Miscible density-stable displacement flows in inclined tube. *Phys. Fluids* **24**, 123102.

ALBA, K., TAGHAVI, S. M. & FRIGAARD, I. A. 2013a Miscible density-unstable displacement flows in inclined tube. *Phys. Fluids* **25**, 067101.

ALBA, K., TAGHAVI, S. M. & FRIGAARD, I. A. 2013b A weighted residual method for two-layer non-Newtonian channel flows: steady-state results and their stability. *J. Fluid Mech.* **731**, 509–544.

ALBA, K., TAGHAVI, S. M. & FRIGAARD, I. A. 2014 Miscible heavy-light displacement flows in an inclined two-dimensional channel: a numerical approach. *Phys. Fluids* **26** (12), 122104.

ASOMAH, A. K. & NAPIER-MUNN, T. J. 1997 An empirical model of hydrocyclones incorporating angle of cyclone inclination. *Miner. Eng.* **10** (3), 339–347.

AUZERAIS, F. M., JACKSON, R. & RUSSEL, W. B. 1988 The resolution of shocks and the effects of compressible sediments in transient settling. *J. Fluid Mech.* **195**, 437–462.

BAIRD, M. H. I., ARAVAMUDAN, K., RAO, N. V. R., CHADAM, J. & PEIRCE, A. P. 1992 Unsteady axial mixing by natural convection in vertical column. *AIChE J.* **38**, 1825–1834.

BENJAMIN, T. B. 1968 Gravity currents and related phenomena. *J. Fluid Mech.* **31**, 209–248.

BIRMAN, V. K., BATTANDIER, B. A., MEIBURG, E. & LINDEN, P. F. 2007 Lock-exchange flows in sloping channels. *J. Fluid Mech.* **577**, 53–77.

BOATENG, A. A. 2015 *Rotary Kilns: Transport Phenomena and Transport Processes*. Butterworth–Heinemann.

BONNECAZE, R. T., HUPPERT, H. E. & LISTER, J. R. 1993 Particle-driven gravity currents. *J. Fluid Mech.* **250**, 339–369.

BORDEN, Z. & MEIBURG, E. 2013 Circulation-based models for Boussinesq internal bores. *J. Fluid Mech.* **726**, R1.

BOYCOTT, A. E. 1920 Sedimentation of blood corpuscles. *Nature* **104**, 532.

COOK, B. P. 2008 Theory for particle settling and shear-induced migration in thin-film liquid flow. *Phys. Rev.* E **78** (4), 045303.

COOK, B. P., ALEXANDROV, O. & BERTOZZI, A. L. 2009 Linear stability of particle-laden thin films. *Eur. Phys. J. Spec. Top.* **166** (1), 77–81.

COOK, B. P., BERTOZZI, A. L. & HOSOI, A. E. 2008 Shock solutions for particle-laden thin films. *SIAM J. Appl. Maths* **68** (3), 760–783.

DAVIES, R. M. & TAYLOR, G. I. 1950 The mechanics of large bubbles rising through extended liquids and through liquids in a tube. *Proc. R. Soc. Lond.* A **200**, 375.

DAVIS, R. H., HERBOLZHEIMER, E. & ACRIVOS, A. 1983 Wave formation and growth during sedimentation in narrow tilted channels. *Phys. Fluids* **26** (8), 2055–2064.

DEBACQ, M., FANGUET, V., HULIN, J. P., SALIN, D. & PERRIN, B. 2001 Self-similar concentration profiles in buoyant mixing of miscible fluids in a vertical tube. *Phys. Fluids* **13**, 3097–3100.

ESPÍN, L. & KUMAR, S. 2014 Forced spreading of films and droplets of colloidal suspensions. *J. Fluid Mech.* **742**, 495–519.

GREENSPAN, H. P. 1978 On the motion of a small viscous droplet that wets a surface. *J. Fluid Mech.* **84** (1), 125–143.

GRUNEWALD, N., LEVY, R., MATA, M., WARD, T. & BERTOZZI, A. L. 2010 Self-similarity in particle-laden flows at constant volume. *J. Engng Maths* **66** (1–3), 53–63.

HALLEZ, Y. & MAGNAUDET, J. 2015 Buoyancy-induced turbulence in a tilted pipe. *J. Fluid Mech.* **762**, 435–477.

HAMED, A. M. 2005 Experimental investigation on the adsorption/desorption processes using solid desiccant in an inclined-fluidized bed. *Renew. Energy* **30** (12), 1913–1921.

HASNAIN, A. & ALBA, K. 2017 Buoyant displacement flow of immiscible fluids in inclined ducts: a theoretical approach. *Phys. Fluids* **29**, 052102.

KERSWELL, R. R. 2011 Exchange flow of two immiscible fluids and the principle of maximum flux. *J. Fluid Mech.* **682**, 132–159.

KURGANOV, A. & TADMOR, E. 2000 New high-resolution central schemes for nonlinear conservation laws and convection–diffusion equations. *J. Comput. Phys.* **160** (1), 241–282.

LYON, M. K. & LEAL, L. G. 1998 An experimental study of the motion of concentrated suspensions in two-dimensional channel flow. Part 1. Monodisperse systems. *J. Fluid Mech.* **363**, 25–56.

MARTIN, J., RAKOTOMALALA, N., TALON, L. & SALIN, D. 2011 Viscous lock-exchange in rectangular channels. *J. Fluid Mech.* **673**, 132–146.

MATA, M. R. & BERTOZZI, A. L. 2011 A numerical scheme for particle-laden thin film flow in two dimensions. *J. Comput. Phys.* **230** (16), 6334–6353.

MATSON, G. P. & HOGG, A. J. 2012 Viscous exchange flows. *Phys. Fluids* **24** (2), 023102.

MAVROMOUSTAKI, A. & BERTOZZI, A. L. 2014 Hyperbolic systems of conservation laws in gravity-driven, particle-laden thin-film flows. *J. Engng Maths* **88** (1), 29–48.

MEIBURG, E. & KNELLER, B. 2010 Turbidity currents and their deposits. *Annu. Rev. Fluid Mech.* **42**, 135–156.

METZGER, B., GUAZZELLI, É. & BUTLER, J. E. 2005 Large-scale streamers in the sedimentation of a dilute fiber suspension. *Phys. Rev. Lett.* **95** (16), 164506.

MURISIC, N., HO, J., HU, V., LATTERMAN, P., KOCH, T., LIN, K., MATA, M. & BERTOZZI, A. L. 2011 Particle-laden viscous thin-film flows on an incline: experiments compared with a theory based on shear-induced migration and particle settling. *Physica* D **240** (20), 1661–1673.

MURISIC, N., PAUSADER, B., PESCHKA, D. & BERTOZZI, A. L. 2013 Dynamics of particle settling and resuspension in viscous liquid films. *J. Fluid Mech.* **717**, 203–231.

NELSON, E. B. & GUILLOT, D. 2006 *Well Cementing*, 2nd edn. Schlumberger Educational Services.

PETITJEANS, P. & MAXWORTHY, T. 1996 Miscible displacements in capillary tubes. Part 1. Experiments. *J. Fluid Mech.* **326**, 37–56.

PHILLIPS, R. J., ARMSTRONG, R. C., BROWN, R. A., GRAHAM, A. L. & ABBOTT, J. R. 1992 A constitutive equation for concentrated suspensions that accounts for shear-induced particle migration. *Phys. Fluids* **4** (1), 30–40.

PRATT, H. R. C. & BAIRD, M. H. I. 1983 Axial dispersion. In *Handbook of Solvent Extraction* (ed. T. C. Lo, M. H. I. Baird & C. Hanson). Wiley.

RICHARDSON, J. F. & ZAKI, W. N. 1954 The sedimentation of a suspension of uniform spheres under conditions of viscous flow. *Chem. Engng Sci.* **3** (2), 65–73.

SAHA, S., SALIN, D. & TALON, L. 2013 Low Reynolds number suspension gravity currents. *Eur. Phys. J.* E **36**, 85.

SAHU, K. C. & VANKA, S. P. 2011 A multiphase lattice Boltzmann study of buoyancy-induced mixing in a tilted channel. *Comput. Fluids* **50** (1), 199–215.

SCHAFLINGER, U., ACRIVOS, A. & ZHANG, K. 1990 Viscous resuspension of a sediment within a laminar and stratified flow. *Intl J. Multiphase Flow* **16** (4), 567–578.

SEBILLEAU, F., ISSA, R. I. & WALKER, S. P. 2016 Analysis of turbulence modelling approaches to simulate single-phase buoyancy driven counter-current flow in a tilted tube. *Flow Turbul. Combust.* **96** (1), 95–132.

SEGRE, G. & SILBERBERG, A. 1961 Radial particle displacements in Poiseuille flow of suspensions. *Nature* **189**, 209–210.

SEON, T., HULIN, J.-P., SALIN, D., PERRIN, B. & HINCH, E. J. 2005 Buoyancy driven miscible front dynamics in tilted tubes. *Phys. Fluids* **17**, 031702.

SEON, T., HULIN, J.-P., SALIN, D., PERRIN, B. & HINCH, E. J. 2006 Laser-induced fluorescence measurements of buoyancy driven mixing in tilted tubes. *Phys. Fluids* **18**, 041701.

SEON, T., ZNAIEN, J., SALIN, D., HULIN, J.-P., HINCH, E. J. & PERRIN, B. 2007*a* Front dynamics and macroscopic diffusion in buoyant mixing in a tilted tube. *Phys. Fluids* **19**, 125105.

SEON, T., ZNAIEN, J., SALIN, D., HULIN, J.-P., HINCH, E. J. & PERRIN, B. 2007*b* Transient buoyancy-driven front dynamics in nearly horizontal tubes. *Phys. Fluids* **19**, 123603.

SHIN, J. O., DALZIEL, S. B. & LINDEN, P. F. 2004 Gravity currents produced by lock exchange. *J. Fluid Mech.* **521**, 1–34.

SPAID, M. A. & HOMSY, G. M. 1996 Stability of Newtonian and viscoelastic dynamic contact lines. *Phys. Fluids* **8** (2), 460–478.

TAGHAVI, S. M., ALBA, K. & FRIGAARD, I. A. 2012*a* Buoyant miscible displacement flows at moderate viscosity ratios and low Atwood numbers in near-horizontal ducts. *Chem. Engng Sci.* **69**, 404–418.

TAGHAVI, S. M., ALBA, K., SEON, T., WIELAGE-BURCHARD, K., MARTINEZ, D. M. & FRIGAARD, I. A. 2012*b* Miscible displacement flows in near-horizontal ducts at low Atwood number. *J. Fluid Mech.* **696**, 175–214.

TAGHAVI, S. M., SEON, T., MARTINEZ, D. M. & FRIGAARD, I. A. 2009 Buoyancy-dominated displacement flows in near-horizontal channels: the viscous limit. *J. Fluid Mech.* **639**, 1–35.

TAGHAVI, S. M., SEON, T., WIELAGE-BURCHARD, K., MARTINEZ, D. M. & FRIGAARD, I. A. 2011 Stationary residual layers in buoyant Newtonian displacement flows. *Phys. Fluids* **23**, 044105.

WANG, L. & BERTOZZI, A. L. 2014 Shock solutions for high concentration particle-laden thin films. *SIAM J. Appl. Maths* **74** (2), 322–344.

WANG, L., MAVROMOUSTAKI, A., BERTOZZI, A. L., URDANETA, G. & HUANG, K. 2015 Rarefaction-singular shock dynamics for conserved volume gravity driven particle-laden thin film. *Phys. Fluids* **27** (3), 033301.

WIKLUND, J. A., STADING, M., PETTERSSON, A. J. & RASMUSON, A. 2006 A comparative study of UVP and LDA techniques for pulp suspensions in pipe flow. *AIChE J.* **52** (2), 484–495.

WONG, J. T. & BERTOZZI, A. L. 2016 A conservation law model for bidensity suspensions on an incline. *Physica* D **330**, 47–57.

ZHENG, Z., RONGY, L. & STONE, H. A. 2015 Viscous fluid injection into a confined channel. *Phys. Fluids* **27** (6), 062105.

ZHOU, J., DUPUY, B., BERTOZZI, A. L. & HOSOI, A. E. 2005 Theory for shock dynamics in particle-laden thin films. *Phys. Rev. Lett.* **94** (11), 117803.

ZNAIEN, J., MOISY, F. & HULIN, J.-P. 2011 Flow structure and momentum transport for buoyancy driven mixing flows in long tubes at different tilt angles. *Phys. Fluids* **23**, 035105.